National Library of Canada
Acquisitions and Bibliographic Services Branch
395 Wellington Street
Ottawa, Ontario
K1A 0N4

Bibliothèque nationale du Canada
Direction des acquisitions et des services bibliographiques
395, rue Wellington
Ottawa (Ontario)
K1A 0N4

Your file - Votre référence

Our file - Notre référence

NOTICE

The quality of this microform is heavily dependent upon the quality of the original thesis submitted for microfilming. Every effort has been made to ensure the highest quality of reproduction possible.

If pages are missing, contact the university which granted the degree.

Some pages may have indistinct print especially if the original pages were typed with a poor typewriter ribbon or if the university sent us an inferior photocopy.

Reproduction in full or in part of this microform is governed by the Canadian Copyright Act, R.S.C. 1970, c. C-30, and subsequent amendments.

AVIS

La qualité de cette microforme dépend grandement de la qualité de la thèse soumise au microfilmage. Nous avons tout fait pour assurer une qualité supérieure de reproduction.

S'il manque des pages, veuillez communiquer avec l'université qui a conféré le grade.

La qualité d'impression de certaines pages peut laisser à désirer, surtout si les pages originales ont été dactylographiées à l'aide d'un ruban usé ou si l'université nous a fait parvenir une photocopie de qualité inférieure.

La reproduction, même partielle, de cette microforme est soumise à la Loi canadienne sur le droit d'auteur, SRC 1970, c. C-30, et ses amendements subséquents.

Canada

UNIVERSITY OF ALBERTA

A SILICA BASED INTEGRATED OPTIC ACCELEROMETER

BY

© MARK ALFRED LANTZ

A thesis submitted to the Faculty of Graduate Studies and Research in partial fulfillment of the requirements for the degree of **MASTER OF SCIENCE**

DEPARTMENT OF ELECTRICAL ENGINEERING

Edmonton, Alberta

FALL 1993

National Library of Canada
Acquisitions and Bibliographic Services Branch
395 Wellington Street
Ottawa, Ontario
K1A 0N4

Bibliothèque nationale du Canada
Direction des acquisitions et des services bibliographiques
395, rue Wellington
Ottawa (Ontario)
K1A 0N4

Your file Votre référence

Our file Notre référence

The author has granted an irrevocable non-exclusive licence allowing the National Library of Canada to reproduce, loan, distribute or sell copies of his/her thesis by any means and in any form or format, making this thesis available to interested persons.

L'auteur a accordé une licence irrévocable et non exclusive permettant à la Bibliothèque nationale du Canada de reproduire, prêter, distribuer ou vendre des copies de sa thèse de quelque manière et sous quelque forme que ce soit pour mettre des exemplaires de cette thèse à la disposition des personnes intéressées.

The author retains ownership of the copyright in his/her thesis. Neither the thesis nor substantial extracts from it may be printed or otherwise reproduced without his/her permission.

L'auteur conserve la propriété du droit d'auteur qui protège sa thèse. Ni la thèse ni des extraits substantiels de celle-ci ne doivent être imprimés ou autrement reproduits sans son autorisation.

ISBN 0-315-88030-9

Canada

UNIVERSITY OF ALBERTA
RELEASE FORM

NAME OF AUTHOR: **MARK ALFRED LANTZ**

TITLE OF THESIS: **A SILICA BASED INTEGRATED OPTIC ACCELEROMETER**

DEGREE: **MASTER OF SCIENCE**

YEAR THIS DEGREE GRANTED: **1993**

Permission is hereby granted to the University of Alberta Library to reproduce single copies of this thesis and to lend or sell such copies for private, scholarly or scientific research purposes only.

The author reserves all other publication and other rights in association with the copyright in the thesis, and except as herein before provided neither the thesis nor any substantial portion thereof may be printed or otherwise reproduced in any material form whatever without the author's prior written permission.

Mark Lantz

Mark Alfred Lantz

5116 - 125 St.
Edmonton, Alberta
Canada

08/09/93
Date

UNIVERSITY OF ALBERTA

FACULTY OF GRADUATE STUDIES AND RESEARCH

The undersigned certify that they have read, and recommend to the Faculty of Graduate Studies and Research for acceptance, a thesis entitled A SILICA BASED INTEGRATED OPTIC ACCELEROMETER submitted by MARK ALFRED LANTZ in partial fulfillment of the requirements for the degree of MASTER OF SCIENCE.

Dr. J. McMullin, Co-Supervisor

Dr. A. M. Robinson, Co-Supervisor

Dr. R. I. MacDonald

Dr. A. W. Lipsett

07/09/93

For Cindy

ABSTRACT

A silica based integrated optic accelerometer has been developed using the facilities of the Alberta Microelectronics Centre. The device was composed of a cantilever beam fabricated from a single mode ridge waveguide. Displacements of the cantilever due to an acceleration of the device result in a change in the optical power output from the device. Optical and mechanical models of the device are presented. The process developed for fabricating single mode ridge waveguides and cantilever waveguides is presented and discussed. Single mode ridge waveguides and cantilever waveguides were fabricated and tested. Results of propagation loss measurements and mode profile measurements on the single mode ridge waveguides are presented as well as results from loss versus displacement measurements of the cantilever waveguides.

ACKNOWLEDGMENTS

I would like to thank my two supervisors, Dr. McMullin and Dr. Robinson, for their advice and encouragement throughout this project, as well as for their financial support. In addition, I would like to thank the staff and students at the AMC materials and devices lab for their instruction and assistance with the facilities at AMC, as well as for their helpful suggestions and advice. I would especially like to thank Alan Mitchell for his assistance with the deposition of materials and his advice in other areas. I would like to thank the AMC for providing generous financial support and access to the excellent facilities. Finally, I would like to thank TR Labs for providing access to testing facilities.

TABLE OF CONTENTS

1 INTRODUCTION 1

2 WAVEGUIDE THEORY AND DESIGN 6
- 2.0 Introduction 6
- 2.1 Dielectric Slab Waveguides 6
  - 2.1.1 Gaussian Approximation of the Fundamental Mode of a Dielectric Slab Waveguide 13
- 2.2 Dielectric Ridge Waveguides 15
  - 2.2.1 Dielectric Ridge Ridge Waveguide Loss Mechanisms 17
- 2.3 Single Mode Ridge Waveguide Coupling Theory 18
- 2.4 Waveguide Design 23

3 CANTILEVER MODELING AND DESIGN 26
- 3.0 Introduction 26
- 3.1 Analytic Mechanical Cantilever Model 26
- 3.2 Accuracy of Model 32
- 3.3 Cantilever Design 32

4 FABRICATION AND PROCESSING 35
- 4.0 Processing Summary 35
- 4.2 Deposition of Core Layer 39
- 4.3 Photolithography 41
  - 4.3.1 Standard Photolithographic Process 42
- 4.4 Reactive Ion Etching 42
- 4.5 Mask Strip and Wafer Clean 44
- 4.6 Waveguide Photolithography 45
  - 4.6.1 Modified Photolithographic Process for Improved Step Coverage 46
- 4.7 Reactive Ion Etch Waveguide Core 46
- 4.8 Mask Strip 47
- 4.9 Flow Waveguide Core 47
- 4.10 Deposition of Silicon Nitride Mask 50
  - 4.10.1 SiN Deposition Process 50

4.11 Undercut Cantilevers in EDP 50
4.11.1 EDP Recipe 53
4.12 Deposition of Upper Cladding Layer 53
4.13 Densification of Upper Cladding Layer 53
4.14 Preparation of Free Standing Cantilevers for Wafer Sawing 54
4.15 Wafer Dicing 54

5 TESTING 55
5.0 Introduction 55
5.1 Waveguide Loss Measurements 55
5.2 Emitted Near Field Pattern Measurements 59
5.3 Emitted Optical Power versus Cantilever Displacement Measurements 62

6 CONCLUSIONS 65

REFERENCES 66

LIST OF FIGURES

Figure 1.0 Optical Accelerometer 1
Figure 1.1 Side View of Integrated Optical Accelerometer 2

Figure 2.0 Light Ray Incident on a Dielectric Interface 6
Figure 2.1 Infinite Dielectric Slab Waveguide 7
Figure 2.2 Graphical Solution of Eq. 2.4 10
Figure 2.3 Electric Field Distribution of Slab Waveguide 10
Figure 2.4 First Four Modes of Slab Waveguide 11
Figure 2.5 Finite Dielectric Slab Waveguide 12
Figure 2.6 Coupling Efficiency of the Fundamental Mode of a Symmetric Slab Wave 14
Figure 2.7a Fundamental Mode of Waveguide and Optimal Gaussian Approximation 15
b Fundamental Mode and 1/e Point Gaussian Approximation 15
Figure 2.8 Rectangular Dielectric Ridge Waveguide 15
Figure 2.9 Approximate Field Distribution in a Ridge Waveguide 16
Figure 2.10 Emission Pattern from a Single Mode Rectangular Waveguide 19

Figure 2.11 Definition of Cantilever Coordinate Systems 19
Figure 2.12 Approximate Intensity Distribution of Waveguide 24
Figure 2.13 Coupling Loss versus Vertical Waveguide Misalignment for a Variety of Reaction of a Cantilever Due to a Motion of its Base 25

Figure 3.0 Reaction of a Cantilever due to a Motion of its Base 26
Figure 3.1 Mode Shapes of First Four Vibrational Modes of a Rectangular Cantilever 28
Figure 3.2 Step Response of Cantilever's Tip due to a 5000 G Acceleration 29
Figure 3.3 Step Response of a 5 x 5 x 500 µm Cantilever to a 5000 G Acceleration 30
Figure 3.4 Cross Section of Cantilever Waveguide 33
Figure 3.5 Tip Deflection versus Acceleration for a : A) 1000 µm Cantilever, B) 700 µm Cantilever, C) 500 µm Cantilever 34

Figure 4.0 Fabrication Summary 35
Figure 4.1 Stabilized Average Refractive Index versus Phosphine Flow (Unannealed) 40
Figure 4.2 Reactive Ion Etching System 43
Figure 4.3 SEM Photo of Step Coverage Defect in Etched Waveguide Core 45
Figure 4.4 Photoresist Mask Thinning due to Step Topography 46
Figure 4.5 SEM Photo of the Waveguide Core Cross Section 47
Figure 4.6 SEM Photo of Bubble Formation due to Excessive Anneal Temperature 49
Figure 4.7 SEM Photo of Waveguide Core After Anneal 49
Figure 4.8 SUPREM Simulation of Phosphorous Diffusion Resulting from Anneal 50
Figure 4.9 Cantilever Undercut Process 51
Figure 4.10 SEM Photo of Free Standing SiO_2 Cantilever Beam 52
Figure 4.11 SEM Photo of Waveguide Core and Surrounding Area After EDP Etch 53
Figure 4.12 SEM Photo of Finished Device 54

Figure 5.1 Waveguide Loss Measurement Setup 56
Figure 5.2 Typical Scattered Light Intensity versus Distance Plot for an Unclad Waveguide 58
Figure 5.3 Typical Scattered Light Intensity versus Distance Plot for a Clad Waveguide before Annealing 58
Figure 5.4 Waveguide Mode Profile Measurement Set Up 60
Figure 5.5 Intensity Plot of the Near Field Image of a Waveguide with an Annealed Upper Cladding Layer 61
Figure 5.6 Intensity Plots of:
A) A Slice along the x-axis of the Image Shown in Figure 5.5 61
B) A Slice along the y-axis of the Image Shown in Figure 5.5 61
Figure 5.7 Cantilever Displacement Test Setup 62
Figure 5.8 Measured and Theoretical Output Power versus Displacement for a Cantilever with a 50 μm Gap 63

LIST OF SYMBOLS

A	area
Å	Angstroms
c	speed of light in vacuum
C	coupling coefficient
cm	centimeters
dB	decibels
dyn	dyne
E	Young's modulus
E_x	electric field
g	grams
G	acceleration of gravity
He	helium
I	second moment of area
kHz	kilohertz
MHz	megahertz
mL	milliliters
mm	millimeters
mTorr	millitorr
n	refractive index
nm	nanometres
nW	nanowatts
N_2	nitrogen
N_2O	nitrous oxide
O_2	oxygen
PH_3	phosphine
Si	silicon
SiH_4	silane
SiO_2	silicon dioxide
T	transmission coefficient
w	beam waist
W	watts
α	attenuation coefficient of waveguide
β	propagation constant of waveguide

∇^2	Laplacian operator
μm	micrometer
μW	microwatt
λ	wavelength of light
η	coupling efficiency
ρ	density
ω	radial frequency
ξ	damping ratio
$^{\circ}C$	degrees Celsius

LIST OF ABBREVIATIONS

AMC	Alberta Microelectronic Centre
BJT	bipolar junction transistor
BOE	buffered oxide etch
CCD	charge coupled device
Ch.	chapter
EDP	ethylene diamine pyrocatacol
Fig.	figure
FWHM	full width half maximum
HMDS	hexamethyldisilazane
min	minute
NA	numerical aperture
PECVD	plasma enhanced chemical vapor deposition
PSG	phosphosilicate glass
psi	pounds per square inch
RF	radio frequency
RIE	reactive ion etching
rpm	revolutions per minute
sccm	standard cubic centimeter per minute
sec	second
Sec.	section
SEM	scanning electron microscope
TE	transverse electric
TM	transverse magnetic
UV	ultraviolet

1 INTRODUCTION

The central goal of this thesis project was to demonstrate the feasibility of fabricating an integrated optic accelerometer using the facilities of the Alberta Microelectronic Centre (AMC). The device was composed of a cantilever beam etched from the center section of a single mode ridge waveguide fabricated on a silicon wafer, see Fig. 1.0.

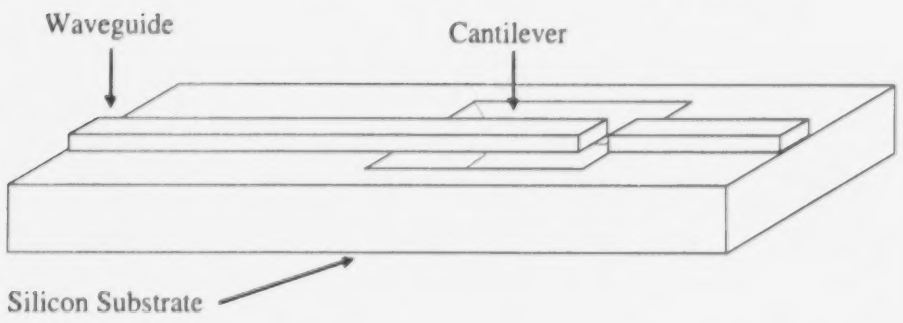

Figure 1.0 Optical Accelerometer

The basic idea behind the device is as follows. Light coupled into one end of the waveguide propagates along the length of the guide and is emitted from the end of the cantilever. In static conditions, the light emitted from the end of the cantilever propagates across the gap and is coupled into the end of the waveguide on the other side. A fraction of the light reaching the end of the cantilever is not coupled into the other waveguide because of partial reflections at the two waveguides ends and because the light beam emitted from the cantilever expands as it propagates across the gap, as illustrated in Fig. 1.1A. When the device is accelerated in a direction perpendicular to the axis of the waveguide, the cantilever bends relative to the waveguide fixed to the substrate, resulting in a reduction in the light coupled into the waveguide across the gap, as shown in Fig 1.1B. In this way, an acceleration will modulate the output power of the device.

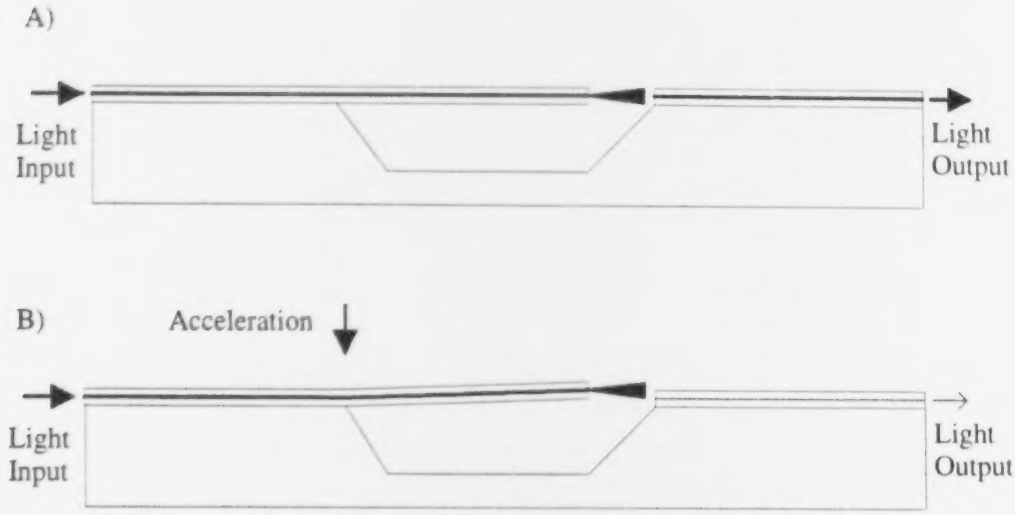

Figure 1.1 Side View of Integrated Optical Accelerometer

A variety of devices which use micromachined cantilevers to measure acceleration have been reported in the literature [1.1-1.8]. The majority of these devices utilize either piezo-resistive, piezo-junction or capacitive techniques to measure acceleration through the measurement of the cantilever's deflection. Recently, however, research on accelerometers using waveguide cantilevers has been reported [1.9-1.11].

Piezo-resistance is an effect which is commonly exploited in strain gauges. Strain in a piezo-resistive material causes a deformation of the crystal lattice which results in a change in the mobility of carriers and a consequent change in the resistance of the material.

Piezo-resistive accelerometers are made by etching a cantilever on or from a silicon substrate. A piezo-resistor is formed on the surface of the cantilever near its base. When the device is accelerated, the cantilever bends, causing stress in the piezo-resistor on the surface of the cantilever. The subsequent change in resistance is proportional to the acceleration of the cantilever. In sensors of this type, a second identical resistor is usually deposited on the supporting substrate and connected in a half bridge configuration with the first resistor in order to convert the change in resistance to a change in voltage. This second resistor can also be used for temperature compensation of the device. Other

designs use four resistors in a full bridge configuration to achieve a resistance-to-voltage conversion and to double the sensitivity of the device.

The characteristics of piezo-resistive accelerometers vary somewhat between the various designs. In general, piezo-resistive accelerometers are relatively easy to fabricate at low cost and are best suited for measuring accelerations in the range of one to several thousand g. The piezo-resistive effect is very sensitive to temperature variations; therefore, devices using this effect require some form of temperature compensation. Accelerometers using the piezo-resistive effect are also sensitive to residual strains in the resistors resulting from the fabrication or packaging process.

Piezo-junction effect accelerometers are similar to piezo-resistive devices, except that they use the piezo-sensitivity of a bipolar junction transistor (BJT) to measure the stress in a bent cantilever, rather than the piezo-resistance effect. Stress in a p-n junction causes a redistribution of the conduction and valance band energy levels, resulting in a change in the minority carrier concentration. The carrier concentration has an exponential dependence on the stress in the junction. Carrier lifetime and mobility are linearly dependent on stress in the junction. At low stress levels, changes in conductivity are dominated by the linear effects, whereas at high stress levels, the exponential effect dominates. In a piezo-junction with a uniform stress on the junction, the transistor's collector current is exponentially dependent on the applied stress. If the collector current is held constant, that is, driven by a constant current source, then the base emitter voltage varies linearly with the applied stress. An acceleration sensor using this phenomenon can be built by fabricating a BJT on the surface of a cantilever, near the base. If the sensor is accelerated, the resulting motion of the cantilever induces a stress in the junction of the BJT which can be measured as a linear change in the base emitter voltage. Accelerometers which use the piezo-junction approach have similar characteristics to piezo-resistive accelerometers except that the former generally have lower power requirements.

Capacitive-based accelerometers measure changes in the capacitance between a fixed metal plate and a moveable metal plate. There are two basic designs. In the first design, a moveable plate suspended by one or more cantilever arms serves as an inertial mass and as one of the plates of a parallel plate capacitor. The movable plate and cantilever arm are etched directly in a silicon wafer. Glass plates are then bonded to both sides of the wafer using field-assisted bonding. Prior to bonding, shallow wells are etched in the glass in the areas which will be directly above and below the movable plate, thus increasing the range of motion of the plate. Thin metal films are deposited onto the bottom of one or both of these wells to serve as the other plate or plates of the capacitor.

Capacitive accelerometers have two possible modes of operation. In the first mode, the plate is free to move as the device is accelerated. Motion of the plate results in a change in the capacitance between the two plates due to the acceleration. In the second mode of operation, an electrostatic force is exerted on the moveable plate by inducing a charge on the plates above and below the movable plate. The capacitive changes resulting when the device is accelerated are used in a control loop to adjust the electrostatic force and balance the acceleration of the plate. The voltage required to balance the acceleration is proportional to the acceleration and can be used as the device output. Operation in the second mode requires metal plates both above and below the movable plate. Sensors operated in this mode are very sensitive but require control circuitry and have a substantially more complex design.

The sensitivity that can be achieved with capacitive-based accelerometers is much higher than can be achieved with piezo-based devices. The sensitivity of capacitive devices is generally limited by an inherent sensitivity to electrical noise and by the capacitance of the conductors used to transmit signals to and from the device. The first problem can be partially overcome by providing shielding for the device. The second problem can be overcome by fabricating active devices on the accelerometer substrate to provide signal amplification. However, this added complexity results in higher costs for accelerometers of this type.

The commercial potential of an integrated optical accelerometer would probably be limited by the cost of the light source and detector. Capacitive and piezo-resistive micro-machined accelerometers have potentially much lower costs. There are, however, several specialized applications for which an optical accelerometer would be well suited. For example, the use of light rather than electricity eliminates the chance of the device causing a spark and makes it ideal for use in explosion-proof environments. Also, the use of optical waveguides makes the device immune to electrical noise which can be a serious problem in capacitive-based accelerometers. This characteristic could make the device useful for vibration monitoring around noise sources such as electric motors. Finally, the use of low loss optical fibers to transmit light to and from the device make it ideal for remote sensing applications such as vibration monitors on oil and gas pipeline booster pumps.

Fulfillment of the goal of this project involved the development of optical and mechanical models of the device, the development of processes to fabricate ridge waveguides and cantilever waveguides, and the testing of these devices. In Chapter 2 of this thesis, a brief review of optical waveguide theory is presented and used to develop models of the field distribution in a ridge waveguide and the coupling loss between two

misaligned ridge waveguides. Following this is a brief discussion of the design of the single mode ridge waveguides used for the device. In the third chapter, a mechanical model of the waveguide cantilever is presented, followed by a discussion of the design of the dimensions of the cantilever. The fourth chapter describes the fabrication processes which were developed to first produce single mode ridge waveguides and then to produce cantilever waveguides. The fifth chapter describes the techniques used to measure the propagation losses and mode profile of the waveguides followed by a presentation of the results of these measurements. This chapter also contains a description of the apparatus used to measure the coupling loss as a function of the displacement of the waveguide cantilevers. The results of these measurements are presented and compared to the loss predicted by the coupling model presented in Chapter 2. In the final chapter, suggestions for the further development of an integrated optical accelerometer are presented.

2 WAVEGUIDE THEORY AND DESIGN

2.0 Introduction

In the first section of this chapter, waveguide theory is briefly reviewed and an exact solution to the slab waveguide problem is presented. The second section describes an approximate solution technique for single mode ridge waveguides based on the slab waveguide solution. Following this is a discussion of loss mechanisms in ridge waveguides. In the third section, the ridge waveguide solution is used to derive an approximate formula for the coupling loss between the ends of two misaligned single mode ridge waveguides. The final section discusses the design of the waveguide used for the accelerometer.

2.1 Dielectric Slab Waveguides

When a light ray is incident on the interface between two dielectric materials, part of the light ray is reflected at the interface and the rest is transmitted through the interface as shown in Fig. 2.0.

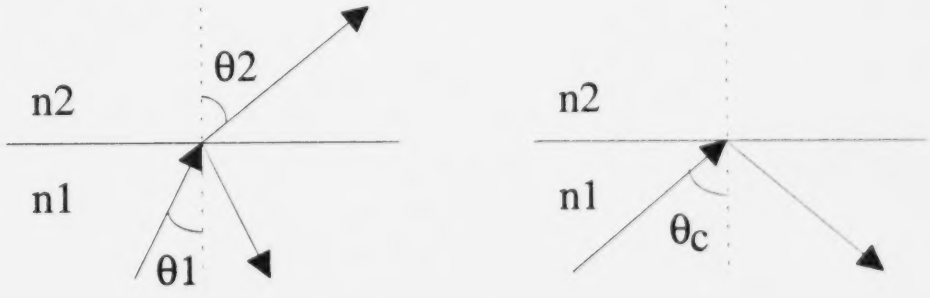

Figure 2.0 Light Ray Incident on a Dielectric Interface

The transmitted ray is refracted at an angle given by Snell's law:

$$n_1 \sin(\theta_1) = n_2 \sin(\theta_2),$$

where n_1 and n_2 are the refractive indices of the two dielectric materials, θ_1 is the angle of incidence of the light ray and θ_2 is the angle of propagation of the refracted ray. If n_1 is

is greater than n_2, an angle θ_1 can be found for which θ_2 equals 90°. This is known as the critical angle. Light incident on a dielectric interface at an angle greater than the critical angle will be completely reflected at the interface. This phenomenon is called total internal reflection. It is the principle used to make dielectric waveguides which confine and guide the propagation of light.

The simplest dielectric waveguide structure is the slab waveguide. It is composed of a layer of dielectric material called the core, sandwiched between two layers of dielectric with smaller refractive indices, called the cladding as illustrated in Fig. 2.1.

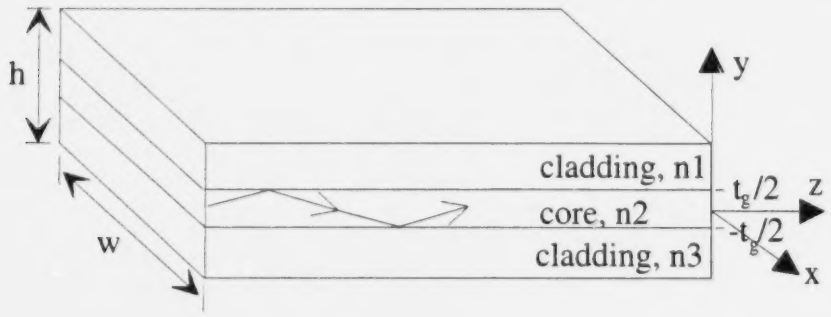

Figure 2.1 Infinite Dielectric Slab Waveguide

The propagation of light in a slab waveguide can be analyzed by solving Maxwell's electromagnetic equations in each of the three regions and then equating the solutions at the boundaries between regions [2.1]. The light wave is assumed to be a coherent plane wave with wavelength λ, propagating in the z direction. In addition, the dimensions h and w are assumed to be infinite.

There are two classes of solutions to Maxwell's equations for this structure: transverse electric (TE) and transverse magnetic (TM). In the TE solution, the electric field vector points in the x direction, whereas in the TM solution, the magnetic field vector points in the x direction. The two solutions are similar and only the TE solution will be treated here. For details of the TM solution the reader is refered to Ref. [2.1].

For the TE case, the derivative of the electric field with respect to x will be zero because there are no changes in the structure in the x direction; that is, $E_x = E_x(y,z,t)$. This allows Maxwell's equations to be reduced to:

$$\nabla^2 E_x = \frac{n_i^2}{c^2}\frac{\partial^2 E_x}{\partial t^2}\ ,\ \ i = 1,2,3 \tag{2.0}$$

where E_x is the electric field, n_i is the refractive index in region i, and c is the speed of light. Eq. (2.0) has solutions of the form:

$$E_x(y,z,t) = \varepsilon_x(y)\exp\{i(\omega t - \beta z) \tag{2.1}$$

where ω is the radial frequency of the plane wave and β is the propagation constant.

In order for the light to be confined to the core region and for Eq. (2.1) to satisfy Eq. (2.0), $\varepsilon_x(y)$ must be a sinusoidal function in the core region and an exponentially decaying function in the cladding regions as given by

$$\varepsilon_x(y) = \left\{ \begin{array}{ll} A\exp\{-q(y-\frac{t_g}{2})\}, & y \geq \frac{t_g}{2} \\ B\cos(hy) + C\sin(hy), & -\frac{t_g}{2} \leq y \leq \frac{t_g}{2} \\ D\exp\{p(y-\frac{t_g}{2})\}, & y \leq -\frac{t_g}{2} \end{array} \right\}, \tag{2.2}$$

where $q = (\beta^2 - n_1^2 k^2)$, $h = (n_2^2 k^2 - \beta^2)$, $p = (\beta^2 - n_3^2 k^2)$ and $k = \frac{2\pi}{\lambda}$.

By equating the electric field at the two boundaries between the core and cladding and by equating the first derivative of the electric field with respect to y at one of the boundaries, the constants A,B,C and D can be related, yielding:

$$\varepsilon_x(y) = \begin{cases} C' \exp\{-q(y - \frac{t_g}{2})\}, & y \geq \frac{t_g}{2} \\ C' [\cos(hy) + \frac{q}{h}\sin(hy)], & -\frac{t_g}{2} \leq y \leq \frac{t_g}{2} \\ C' [\cos(h\frac{t_g}{2}) + \frac{q}{h}\sin(h\frac{t_g}{2})] \exp\{p(y - \frac{t_g}{2})\}, & y \leq -\frac{t_g}{2} \end{cases}, \qquad (2.3)$$

where the value of C' is dependent on the intensity of the plane wave and is generally normalized to yield a maximum electric field of 1. By combining Eqs. (2.0), (2.1) and (2.3) and then equating the derivative of the electric field with respect to y at the other boundary, an equation determining the value of β can be found:

$$\tan(ht_g) = \frac{p+q}{h\left(1 - \frac{pq}{h^2}\right)} \qquad (2.4)$$

Eq. (2.4) is a transcendental equation and can be solved either numerically or graphically. In the graphical approach, both sides of the equation are plotted as a function of β. The intersection(s) of these curves yield the value(s) of β. In Fig. 2.2, both sides of Eq. (2.4) are plotted for a slab waveguide with: $n_1 = n_3 = 1.4585$, $n_2 = 1.462$, $t_g = 2\ \mu m$, $\lambda = 670$ nm. For this example, there is only one possible solution to Eq. (2.4): $\beta \approx 1.3692 \times 10^7\ m^{-1}$. Taking this as the value of β, the electric field distribution for this waveguide is plotted in Fig. 2.3.

As the five constants: n_1, n_2, n_3, t_g and λ, are varied, the number of solutions to Eq. (2.4) varies. Each solution corresponds to a unique electric field distribution called a mode. Light confined in a waveguide will be distributed in one of its modes or in a combination of them. The example waveguide used for Figs. 2.2 and 2.3 is called a single moded waveguide because only one solution to Eq. (2.4) exists for this guide.

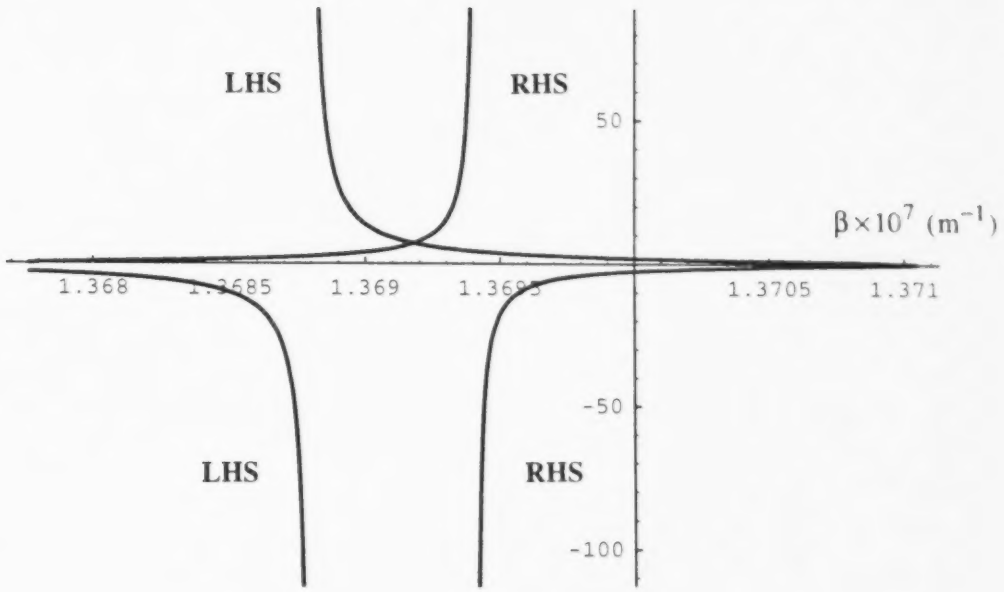

Figure 2.2: Graphical Solution of Eq. 2.4 ($\beta \approx 1.3692 \times 10^7$ m^{-1})
($n_1 = n_3 = 1.4585$, $n_2 = 1.462$, $t_g = 2$ μm, $\lambda = 670$ nm)

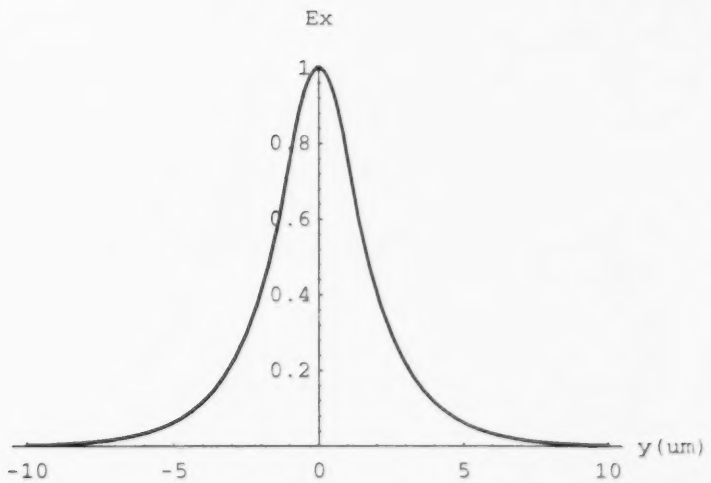

Figure 2.3: Electric Field Distribution of Slab Waveguide ($\beta \approx 1.3692 \times 10^7$ m^{-1})

If the thickness of the core in this example were increased, the number of modes would increase and the guide would become multi-moded. For example, if the width of this waveguide were increased to 20 μm, then Eq. (2.4) would have six solutions and the guide would have six modes. The first four of these modes are plotted in Fig. 2.4. The lowest order or fundamental mode is approximately Gaussian in shape. Each higher order mode is characterized by an additional crossing of the y-axis.

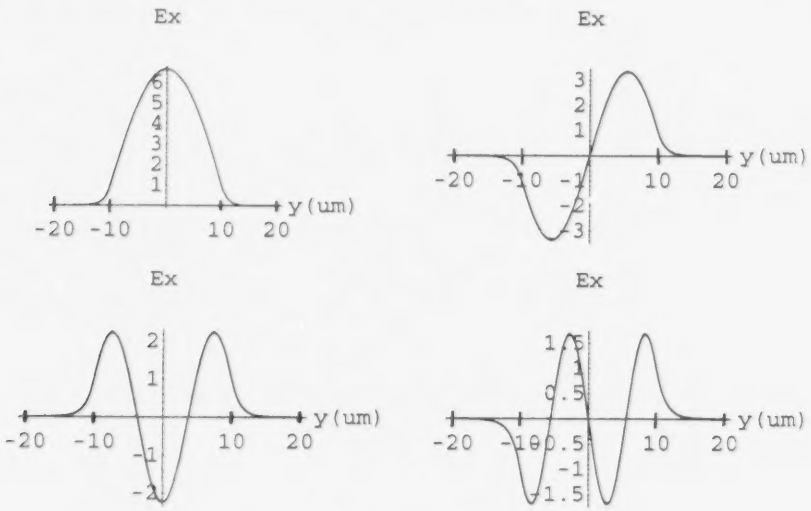

Figure 2.4 : First Four Modes of Slab Waveguide
(n_1= n_3= 1.4585, n_2= 1.462, t_g= 20 μm, λ= 670 nm)

If the wavelength of light propagating in the example waveguide is increased and the other parameters are fixed, the number of modes decreases. The maximum wavelength for which a given mode will propagate is called the cut-off wavelength for that mode and is designated λ_c.

If the difference between the refractive index of the core and cladding layers is increased, the number of modes of the waveguide also increases and the penetration of the electric field into the cladding layers decreases. Waveguides with equal refractive indices in the upper and lower cladding layers are called symmetric waveguides. Waveguides with unequal cladding indices are called asymmetric waveguides. The electric field distribution in an asymmetric waveguide is shifted towards the cladding layer with the higher refractive index. Symmetric slab waveguides will always have at least one propagation mode, as long as the core refractive index is larger than that of the cladding refractive index. Asymmetric waveguides, however, do not always have a fundamental propagation mode [2.1]. For a given core thickness and combination of

refractive indices, there will be a cutoff wavelength in an asymmetric waveguide for which light of a larger wavelength will not be confined to the core.

The electric field which penetrates into the cladding of the waveguide is called the evanescent field or the evanescent tail of the mode. Although the electric field penetrates into the cladding, the net power flow into the cladding is zero. This phenomenon is analogous to imaginary power flow in a transmission line. The power flow is positive during one half cycle and negative during the other, resulting in a zero net power flow into the cladding and confinement of the light to the core region.

The infinite geometry assumed in the above analysis of a dielectric slab waveguide, is of course, not physically realizable. A more practical slab waveguide is depicted in Fig. 2.5.

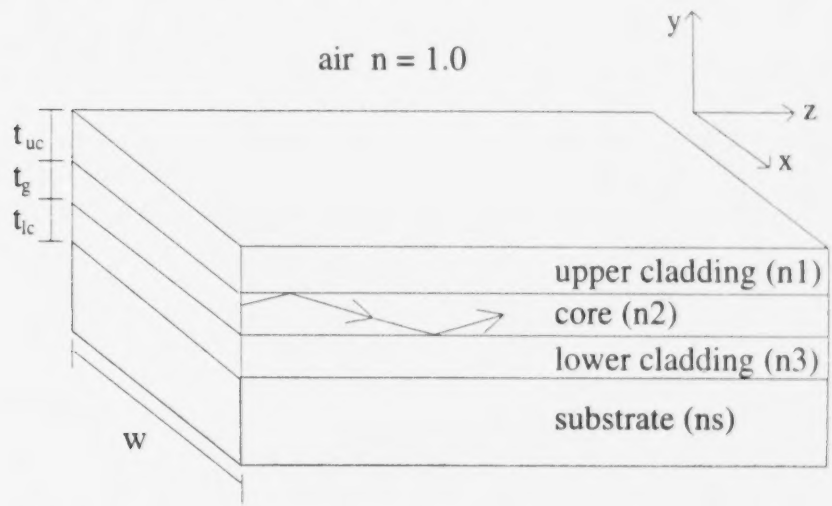

Figure 2.5 Finite Dielectric Slab Waveguide

In this type of waveguide, the dimensions of the core and cladding layers: t_{uc}, t_g, t_{lc}, and w are finite. The solution to Maxwell's equations for this structure is well approximated by the solution to an infinite dielectric slab waveguide, if the following two conditions are met. First, the light beam propagating in the guide must be narrower than the width of the guide and not spread out enough to reflect off the sides of the guide. Second, the thicknesses of the two cladding layers must be large compared to the wavelength of light propagating in the guide. Because the cladding layers are not infinite, some of the evanescent field will penetrate into the regions above and below the cladding layers. If

the refractive index in these regions is larger than or equal to that of the core layer, the evanescent field which penetrates into these regions will be coupled into radiative modes and will be lost. In general, only the substrate material has a larger refractive index than that of the core. Losses resulting from leakage into the substrate are called substrate losses. In order to minimize these losses, the thickness of the lower cladding layer must be made large enough so that the evanescent field will decay to a negligible magnitude before it penetrates into substrate.

2.1.1 Gaussian Approximation of the Fundamental Mode of a Dielectric Slab Wave Guide

The fundamental mode of a symmetric slab waveguide is similar in shape to a Gaussian function. Although the actual mode shape is not Gaussian, a Gaussian function is much simpler and makes a useful approximation; specifically we take

$$\varepsilon_x{}^2(y) \approx \varepsilon_0 \exp\left\{-\frac{y^2}{w^2}\right\}. \tag{2.5}$$

The shape of a Gaussian distribution is characterized by the single parameter w. At y = w, the square of the electric field drops to 1/e of its maximum value. ε_0 is dependent on the intensity of the plane wave and is generally normalized to 1. One approach to approximating a slab waveguide's fundamental mode with a Gaussian function is to use the 1/e point of the actual mode for the value of w. In general, however, this does not yield the optimum approximation. A better approach is to find the value of w which yields the maximum coupling efficiency, η, of the waveguide mode into a Gaussian distribution. The coupling efficiency is defined as the superposition of the light power in the waveguide mode onto the Gaussian mode profile [2.2]. Specifically

$$\eta = \frac{\left|\int_{-\infty}^{\infty} \Gamma_{wg} \cdot \Psi^*_{gauss}\, dy\right|^2}{\left[\int_{-\infty}^{\infty} \Gamma_{wg} \cdot \Gamma^*_{wg}\, dy\right]\left[\int_{-\infty}^{\infty} \Psi_{gauss} \cdot \Psi^*_{gauss}\, dy\right]}, \tag{2.6}$$

where Γ_{wg} is the intensity distribution of the waveguide mode, Ψ_{gauss} is the intensity distribution of the Gaussian approximation and * is the complex conjugate. If the waveguide is symmetric, then Eq. (2.6) reduces to:

$$\eta = \frac{\left[\int_0^\infty \varepsilon_{wg}^2(y)\cdot\varepsilon_{gauss}^2(y)dy\right]^2}{\left[\int_0^\infty \varepsilon_{wg}^2(y)dy\right]^2\left[\int_0^\infty \varepsilon_{gauss}^2(y)dy\right]^2}, \tag{2.7}$$

where, ε_{wg} is the actual electric field distribution in the y-direction and ε_{gauss} is the Gaussian approximation to the electric field distribution in the y-direction. By plotting the coupling efficiency as a function w, the value of w which yields the best approximation can be found. This is done in Fig. 2.6 for a sample waveguide with the following parameters: t_g = 2 μm, $n_1 = n_3$ = 1.4585, n_2 = 1.4620. The 1/e point of the fundamental mode of this waveguide occurs at w = 1.58 μm. If this is taken as the value of w, a coupling efficiency of 99.2% is achieved. However, the optimum coupling of 99.6% occurs at a value of w = 1.43 μm.

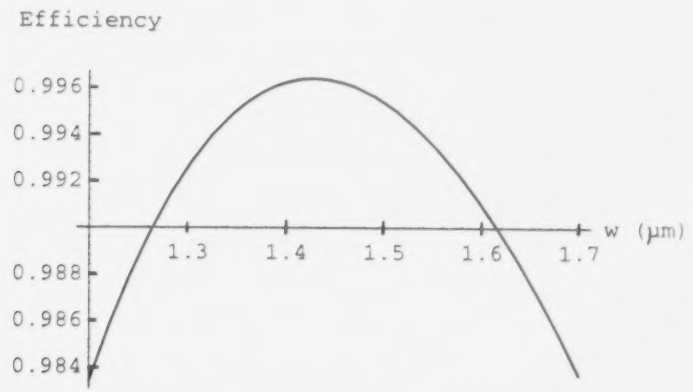

Figure 2.6: Coupling Efficiency of the Fundamental Mode of a Symmetric Slab Waveguide into a Gaussian Distribution (t_g = 2 μm, $n_1 = n_3$ = 2.4585, n_2 = 2.4620)

In Fig. 2.7A, the fundamental mode of this waveguide is plotted over the optimal Gaussian approximation. In Fig. 2.7B, the fundamental mode is plotted over the 1/e point Gaussian approximation.

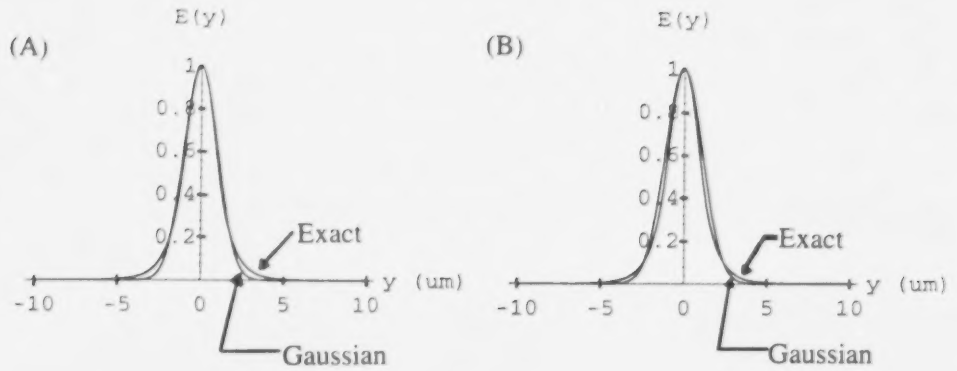

Figure 2.7A: Fundamental Mode of Waveguide and Optimal Gaussian Approximation
B: Fundamental Mode and 1/e Point Gaussian Approximation

2.2 Dielectric Ridge Waveguides

The dielectric slab waveguide is limited in its useful applications because it only provides light confinement in one dimension. A more practical guide, with confinement in two dimensions, can be achieved by making the core width smaller and surrounding the sides of the core with cladding layers as illustrated in Fig. 2.8. Waveguides with this geometry are called embedded rectangular ridge waveguides.

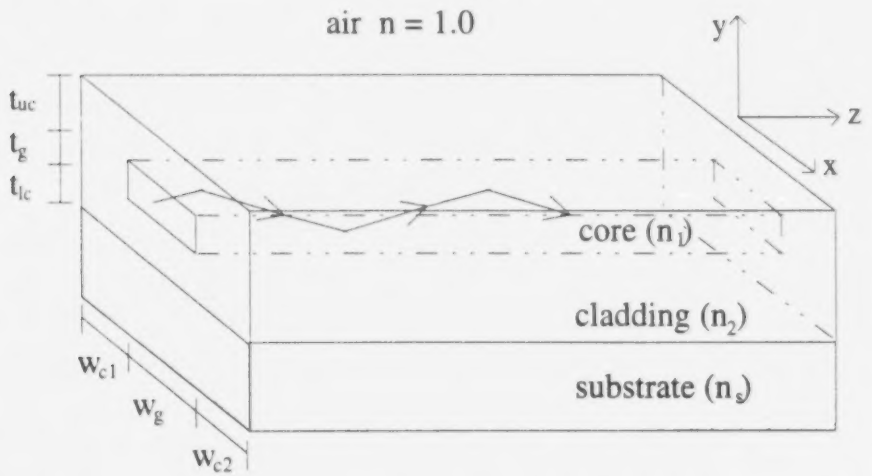

Figure 2.8 Rectangular Dielectric Ridge Waveguide

The propagation of light in a ridge waveguide is more difficult to analyze than propagation in a slab waveguide. The analysis of the slab waveguide was simplified by the assumption of infinite geometry in the x and y directions. For the structure depicted in Fig. 2.8, reflections can occur in two dimensions and a solution to Maxwell's equations of the form: E = E(x,y,z,t) is expected. It is not possible to obtain a closed form solution to Maxwell's equations for this problem; however, several approximate solution techniques of varying complexity are available.

If the ridge waveguide is symmetric, then the simplest approach is to approximate the x and y variation of the fundamental mode as Gaussian,

$$\varepsilon^2(x,y) \approx \varepsilon_0 \exp\left\{-\frac{x^2}{w_x^2}\right\}\exp\left\{-\frac{y^2}{w_y^2}\right\}. \qquad (2.8)$$

The parameters w_x and w_y can be approximated as the Gaussian fit to a slab waveguide with similar parameters as indicated in Fig. 2.9.

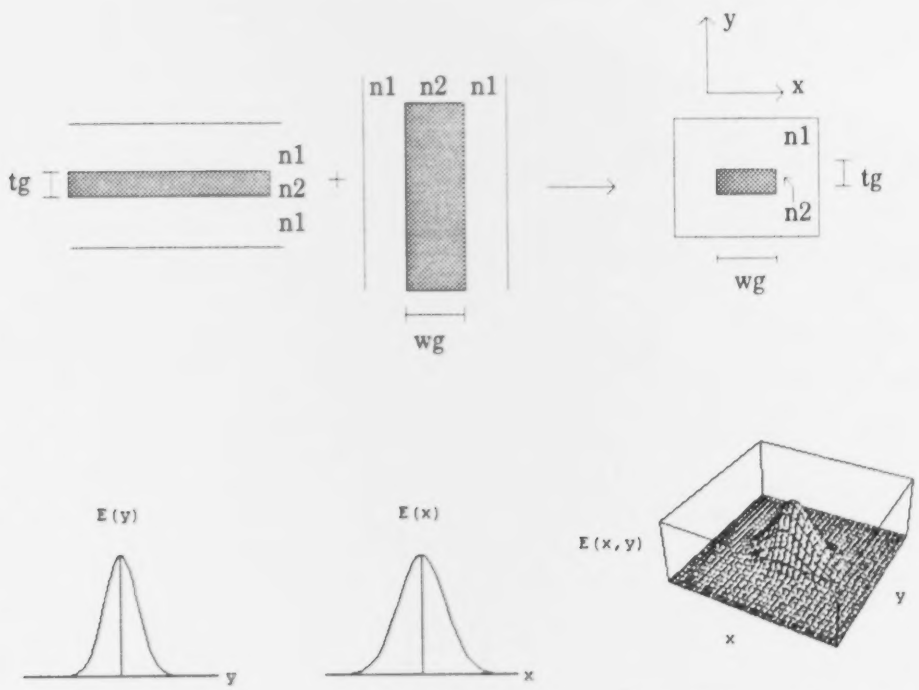

Figure 2.9 Approximate Field Distribution in a Ridge Waveguide
($w = 5\ \mu m$, $t_g = 2\ \mu m$, $n_1 = 1.4585$, $n_2 = 1.462$, $\lambda = 670$ nm)

2.2.1 Dielectric Ridge Waveguide Loss Mechanisms

In the waveguide analysis of Secs. 2.1 and 2.2, the light confined within the waveguide was assumed to propagate without loss. Physically-realizable waveguides are not, however, lossless. As light propagates through a waveguide, the intensity of the light decreases because of a variety of phenomena. In general, the light power propagating in a waveguide decreases exponentially with distance traveled,

$$P = P_0 \exp(-\alpha z), \tag{2.9}$$

where P_0 is the power in the waveguide at $z = 0$ and α is the attenuation coefficient.

Losses in straight dielectric ridge waveguides result from three mechanisms: absorption, scattering and substrate radiation. Absorption losses result when photons propagating in the waveguide are absorbed by the waveguide material. Absorption is caused by a variety of mechanisms, but can be minimized through the selection of core and cladding materials and the wavelength of light used. Scattering losses can be divided into two categories: imperfection scattering and surface scattering. Imperfection scattering losses result when photons are scattered by imperfections such as contaminant particles, low density regions or voids in the core and cladding material. Losses due to imperfections increase as the size and/or number of imperfections increase. For good quality materials, imperfection scattering losses are negligible compared to surface scattering losses. Surface scattering losses result from photons being scattered by roughness in the core-cladding interface. Losses due to surface scattering depend on the size of the surface variations relative to the wavelength of light propagating in the guide. Surface scattering losses can be minimized by minimizing the roughness in the core-cladding interface. Substrate radiation losses result when the evanescent field penetrates through the cladding layers into a substrate material with a refractive index equal to or greater than the core material, as previously discussed at the end of Sec. 2.1. Radiation losses can be minimized by selecting the thicknesses and refractive indices of the core and cladding layers and the wavelength of light, such that the evanescent field decays to a negligible value before it penetrates into the substrate.

2.3 Single Mode Ridge Waveguide Coupling Theory

The radiation pattern emitted from the end of a single mode rectangular waveguide can be modeled as an elliptical Gaussian beam, using a scalar field approximation [2.3]. With reference to Fig. 2.10 this is given by

$$\frac{E(x,y,z)}{E_0} = \left(\frac{w_{ox}w_{oy}}{w_x(z)w_y(z)}\right)^{1/2} \exp\left\{\frac{-x^2}{w_x^2(z)} - j\frac{kx^2}{2R_x(z)}\right\} \exp\left\{\frac{-y^2}{w_y^2(z)} - j\frac{ky^2}{2R_y(z)}\right\} \exp\left\{-j\left[kz - \tan^{-1}\left(\frac{z}{z_o}\right)\right]\right\}, \tag{2.10}$$

where

$$w_x^2(z) = w_{ox}^2\left[1+\left(\frac{z}{z_{ox}}\right)^2\right], \qquad w_y^2(z) = w_{oy}^2\left[1+\left(\frac{z}{z_{oy}}\right)^2\right],$$

$$z_{ox} = \frac{\pi n w_{ox}^2}{\lambda_o}, \qquad z_{oy} = \frac{\pi n w_{oy}^2}{\lambda_o},$$

$$R_x(z) = z\left[1+\left(\frac{z_{ox}}{z}\right)^2\right], \qquad R_y(z) = z\left[1+\left(\frac{z_{oy}}{z}\right)^2\right], \text{ and}$$

w_{ox} is the beam waist in the x direction, w_{oy} is the beam waist in the y direction, λ_o is the free space wavelength of light and n is refractive index of medium.

If the light emitted from the end of a waveguide is incident on the end of another waveguide, a fraction of the incident light can be coupled into the second waveguide. The transmission coefficient, T, is defined as the total power coupled from the first waveguide into propagating modes in the second waveguide, divided by the total power propagating in the first waveguide. The transmission coefficient is strongly dependent on the lateral, axial and angular alignment of the two waveguide ends.

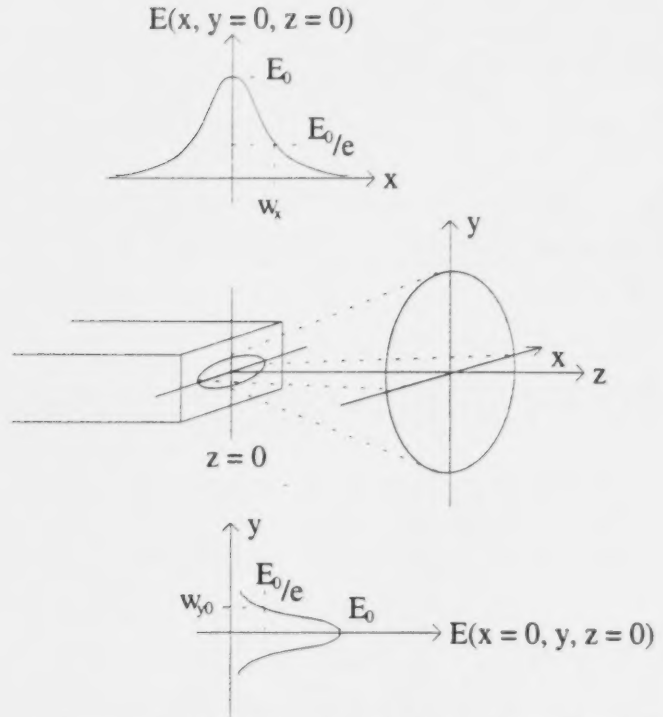

Figure 2.10 Emission Pattern from a Single Mode Rectangular Waveguide

For the case of the proposed optical accelerometer, misalignments in the y and z directions must be considered as shown in Fig. 2.11.

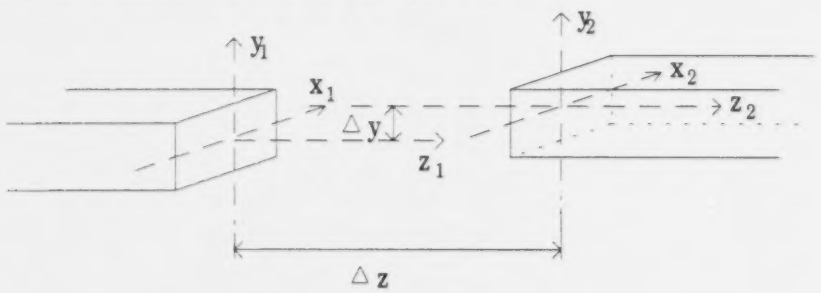

Figure 2.11 Definition of Cantilever Coordinate System

Angular misalignment between the faces of the waveguides is negligible compared to the y and z misalignments and therefore need not be considered. The transmission coefficient as a function of the two misalignments, Δy and Δz can be derived as follows using the approach of Nemoto and Makimoto to calculate the coupling between optical fibers [2.4].

The field emitted from waveguide 1 can be approximated as

$$\frac{E_1(x_1,y_1,z_1)}{E_{01}} = \left(\frac{w_{ox1}w_{oy1}}{w_{x1}(z_1)w_{y1}(z_1)}\right)^{1/2} \exp\left\{\frac{-x_1^2}{w_{x1}^2(z_1)} - j\frac{kx_1^2}{2R_{x1}(z_1)}\right\}$$
$$\exp\left\{\frac{-y_1^2}{w_{y1}^2(z_1)} - j\frac{ky_1^2}{2R_{y1}(z_1)}\right\}\exp\left\{-j\left[kz_1 - \tan^{-1}\left(\frac{z_1}{z_{o1}}\right)\right]\right\}. \qquad (2.11)$$

Similarly, the mode field at waveguide 2 can be approximated as

$$\frac{E_2(x_2,y_2,z_2)}{E_{02}} = \left(\frac{w_{ox2}w_{oy2}}{w_{x2}(z_2)w_{y2}(z_2)}\right)^{1/2} \exp\left\{\frac{-x_2^2}{w_{x2}^2(z_2)} - j\frac{kx_2^2}{2R_{x2}(z_2)}\right\}$$
$$\exp\left\{\frac{-y_2^2}{w_{y2}^2(z_2)} - j\frac{ky_2^2}{2R_{y2}(z_2)}\right\}\exp\left\{-j\left[kz_2 - \tan^{-1}\left(\frac{z_2}{z_{o2}}\right)\right]\right\}. \qquad (2.12)$$

The following can be used to transform the Eq. (2.12) into the same coordinate system as Eq. (2.11).

$$x_1 = x_2 \qquad (2.13)$$
$$y_1 = y_2 + \Delta y \qquad (2.14)$$
$$z_1 = z_2 + \Delta z \qquad (2.15)$$

If reflection losses at the ends of the waveguides are ignored, Eq. (2.16) below, can be used to calculate the coupling coefficient between the two waveguides and Eq. (2.17) can be used to calculate the transmission coefficient between the two waveguides.

$$C = \frac{\int_{-\infty}^{\infty}\int_{-\infty}^{\infty} E_1(x_2, y_2, z_2) E_2^*(x_2, y_2, z_2) dx_2 dy_2}{\int_{-\infty}^{\infty}\int_{-\infty}^{\infty} E_1(x_1, y_1, z_1) E_1^*(x_1, y_1, z_1) dx_1 dy_1}, \tag{2.16}$$

$$T = |C|^2. \tag{2.17}$$

If the waveguides are assumed to be identical, then

$$w_{0x1} = w_{0x2} = w_{0x}, \tag{2.18}$$

$$w_{0y1} = w_{0y2} = w_{0y}. \tag{2.19}$$

After much algebra, the transmission coefficient resulting from the two misalignments reduces to

$$T = \frac{1}{\left[\left(1+\left(\frac{\Delta z}{2z_{0x}}\right)^2\right)\left(1+\left(\frac{\Delta z}{2z_{0y}}\right)^2\right)\right]^{1/2}} \exp\left\{-\frac{\Delta y^2}{w_{0y}^2\left(1+\left(\frac{\Delta z}{2z_{0y}}\right)^2\right)}\right\}. \tag{2.20}$$

The transmission coefficient accounting for reflection losses is given by [2.2]

$$T_{reflections} = \left[\frac{4 n_{core} n_0}{(n_{core} + n_0)^2}\right]^2, \tag{2.21}$$

where n_{core} is the refractive index of the waveguide core and n_0 is the refractive index of the region between the two waveguides. The total transmission coefficient is given by the product of Eqs. (2.20) and (2.21)

$$T_{total} = \frac{\left[\frac{4n_{core}n_0}{(n_{core}+n_0)^2}\right]^2}{\left[\left(1+\left(\frac{\Delta z}{2z_{0x}}\right)^2\right)\left(1+\left(\frac{\Delta z}{2z_{0y}}\right)^2\right)\right]^{1/2}} \exp\left\{-\frac{\Delta y^2}{w_{0y}^2\left(1+\left(\frac{\Delta z}{2z_{0y}}\right)^2\right)}\right\}. \quad (2.22)$$

Eq. (2.22) reduces to the result obtained by Nemoto and Makimoto [2.4] for the case of circular symmetry, i.e. $w_{0x} = w_{0y} = w_0$.

The loss in dB due to the misalignments Δy and Δz and to reflections is given by

$$L = -10\log_{10}(T_{total}). \quad (2.23)$$

2.4 Waveguide Design

The starting point of the waveguide design was the decision to use a single mode waveguide in order to achieve predictable coupling across the gap in the guide. The second design decision was to use a visible light source to simplify the testing of the device. A 675 nm semiconductor laser diode was selected. Corning Flexor 850 optical fiber was then selected to transmit light from the source to the device. This fiber is single moded at 675 nm, has a numerical aperature (N.A.) of 0.1 and a core diameter of 5 μm.

The coupling loss between the fiber and the waveguide can be minimized by designing the waveguide to have a mode profile similar to that of the fiber. A simple way to achieve this is to match the N.A. and the core dimensions of the waveguide to those of the fiber. As will be seen in Sec. 4.1, the refractive index of the undoped SiO_2 cladding layer was 1.456. Therefore, a core index of 1.460 was required to achieve the desired N.A. A core width of 5 μm and a thickness of 3 μm was decided upon as a compromise amoung coupling, sensitivity and fabrication considerations. A 5 μm core thickness would have resulted in better coupling but would have created fabrication problems and reduced the sensitivity of the device for a fixed length of cantilever. The design of the thickness of the upper and lower cladding layers also required a compromise between waveguide loss, sensitivity and fabrication considerations. The thickness of the lower cladding layer was set at 4 μm and the thickness of the upper cladding layer was set at 3 μm.

The intensity distribution of this structure was calculated using the slab waveguide approximation presented in Sec. 2.2. The equivalent slab waveguide modes are plotted in Fig. 2.12A. The Gaussian approximation of these modes are plotted in Fig. 2.12B. The optimum approximation in the x direction occurs at an intensity beam waist of $w_x = 2.010$ with an efficiency of $\eta = 99.86\%$. The optimum approximation in the y direction occurs at an intensity beam waist of $w_y = 1.516$ at an efficiency of $\eta = 99.95\%$. The approximate two-dimensional intensity distribution, based on the Gaussian slab approximations, is plotted in Fig. 2.12C.

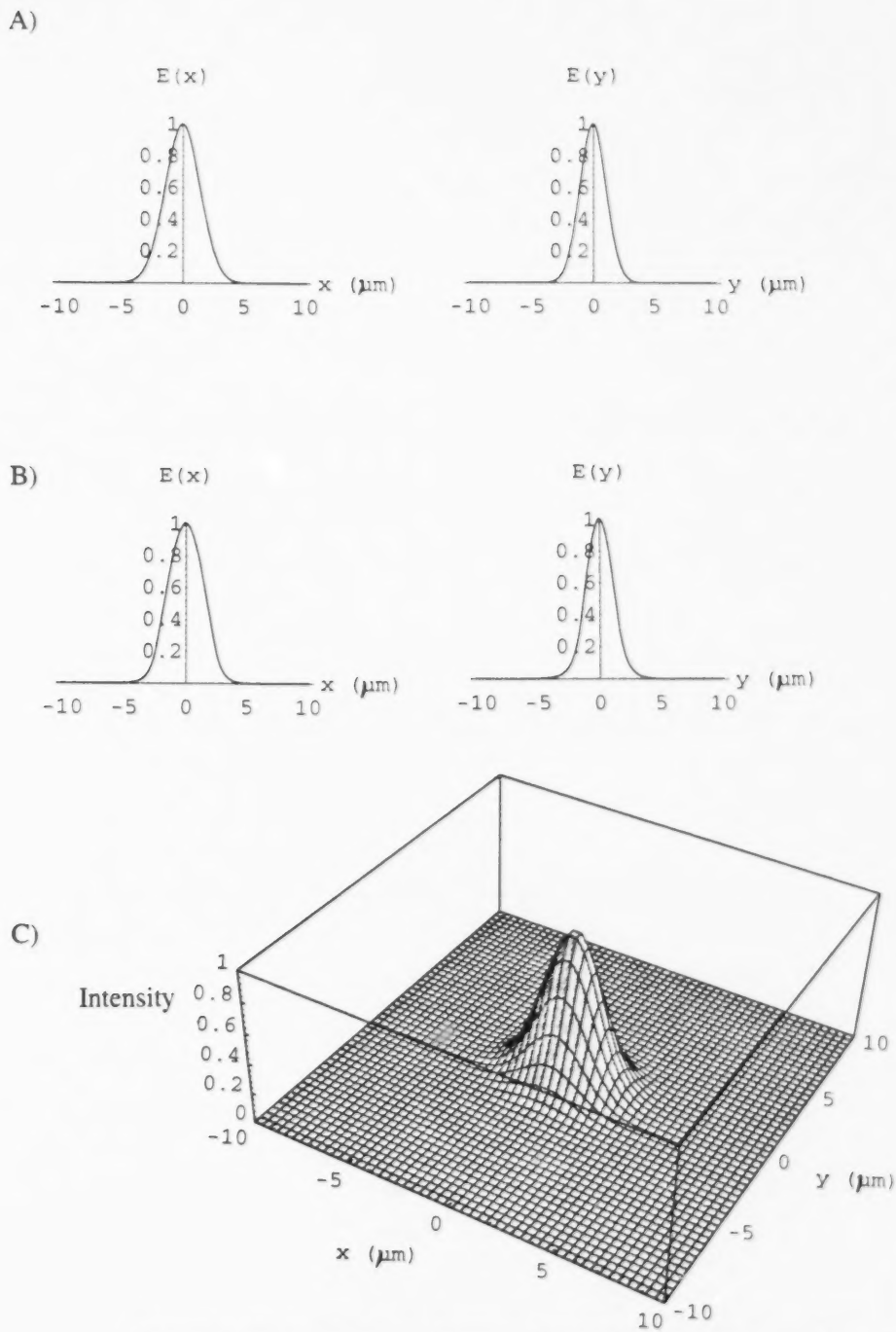

Figure 2.12 Approximate Intensity Distribution of Waveguide

A) Slab Waveguide Solution Electric Field Distributions

B) Gaussian Approximation to Slab Waveguide Solutions

C) Gaussian Approximation to Ridge Waveguide

The coupling loss versus vertical displacement was calculated for a range of gap sizes using the approximate field distribution shown in Fig. 2.12 and Eqs. (2.22) and (2.23). The results of this analysis are presented in Fig. 2.13. The accelerometer dynamic range which can be achieved with this waveguide design depends on the maximum allowable coupling loss. The maximum allowable coupling loss, in turn, depends on a variety of factors, such as the source power, the detector noise floor, the loss in the waveguide and in the input and output fibers as well as the coupling loss at the fiber waveguide interfaces. For a fixed allowable loss, the acceleration range over which the device would be sensitive can be increased at the expense of the device sensitivity, by increasing the width of the gap.

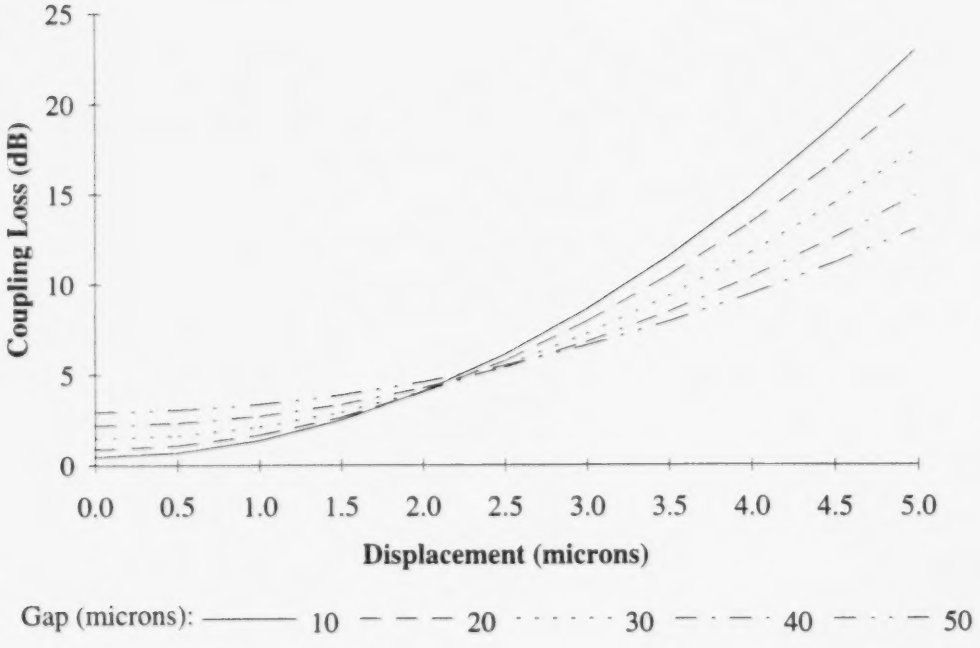

Figure 2.13 Coupling Loss versus Vertical Waveguide Misalignment for a Variety of Gap Sizes

3 CANTILEVER MODELING AND DESIGN

3.0 Introduction

In Section 3.1 of this chapter, a mechanical model of the proposed waveguide-cantilever structure is presented. In Section 3.2, this model is compared to a finite element model generated using the software package ANSYS. The final section of this chapter discusses the design of the cantilever and the results obtained by modeling the dynamic behavior of this design with the model presented in Sec. 3.1.

3.1 Analytic Mechanical Cantilever Model

Modeling the reaction of a cantilever to an acceleration of its base is a classical problem in mechanical engineering [3.1-3.3]. The displacement of a cantilever relative to its base, w_r, due to a motion of its base w_b, is described by the following fourth order partial differential equation:

$$\rho(x)A(x)\frac{\partial^2 w_r(x,t)}{\partial t^2}+\frac{\partial^2}{\partial x^2}[E(x)I(x)\frac{\partial^2 w_r(x,t)}{\partial x^2}]=-\rho(x)A(x)\frac{d^2 w_b(t)}{dt^2}, \quad (3.1)$$

where $\rho(x)$ is the density of the cantilever material, $A(x)$ is the cross sectional area of the cantilever, $E(x)$ is Young's modulus of the cantilever material and $I(x)$ is the second moment of area of the cantilever's cross section. As indicated in Fig. 3.0, the absolute displacement of the cantilever is $w_a(t)$ and is obviously $w_a(t) = w_b(t) + w_r(x,t)$. (3.2)

Figure 3.0 Reaction of a Cantilever Due to a Motion of its Base

For a uniform cantilever ρ(x), A(x), E(x) and I(x) are all constants and Eq. (3.1) reduces to

$$\rho A \frac{\partial^2 w_r(x,t)}{\partial t^2} + EI \frac{\partial^4 w_r(x,t)}{\partial x^4} = -\rho A \frac{d^2 w_b(t)}{dt^2} \tag{3.3}$$

For a rectangular cross section, $I = \frac{1}{12} bh^3$, where b is the width and h is the thickness.

The derivation of Eq. (3.3) neglects rotatory inertia and shear deflection, an approximation which is valid for small deflections of the beam. The derivation uses the Euler-Bernoulli beam theory relation between bending moment and curvature, a relation that is valid for the lower order modes of vibration of beams that are long relative to their thickness. The following solution to Eq. (3.1) is therefore only valid within the range of these approximations.

The solution to Eq. (3.3) can be found using the separation of variables technique. The resulting solution assuming an acceleration of the base in the y direction and using the boundary conditions of zero bending moment and shear force at the beam's tip and zero deflection and slope at the beam's fixed end, is [3.3]

$$w(x,t) = \sum_{n=1}^{\infty} W_n(x) T_n(t), \tag{3.4}$$

where n is the so called mode number,

$W_n(x) = \sin(\beta_n x) - \sinh(\beta_n x) - \alpha_n[\cos(\beta_n x) - \cosh(\beta_n x)]$ and

$T_n(t) = \frac{c_n}{b_n}[\cos(\omega_n t) - 1]$.

The β_n are defined by $\left[\cos(\beta L)\cosh(\beta L) = -1, \left\{\beta_1 = \frac{1.875104}{L}, \beta_2 = \frac{4.694091}{L}, \ldots\right\}\right]$ (3.5)

The natural resonant frequency of the nth mode in rad/ sec is $\omega_n = \beta^2_n \sqrt{\frac{EI}{\rho A}}$, (3.6)

Also $\alpha_n = \frac{\sin(\beta_n x) + \sinh(\beta_n x)}{\cos(\beta_n x) + \cosh(\beta_n x)}$, $c_n = \rho A \frac{d^2 w_b(t)}{dt^2} \int_0^L W_n(x)dx$, and $b_n = EI\beta_n{}^4 \int_0^L W^2{}_n(x)dx$.

The mode shapes for the first four modes of vibration are plotted in Fig. 3.1. For excitations of the base below the first resonant frequency the amplitudes of the modes

decrease rapidly with increasing mode number. Thus, Eq. (3.4) can be accurately approximated by summing only the first few modes.

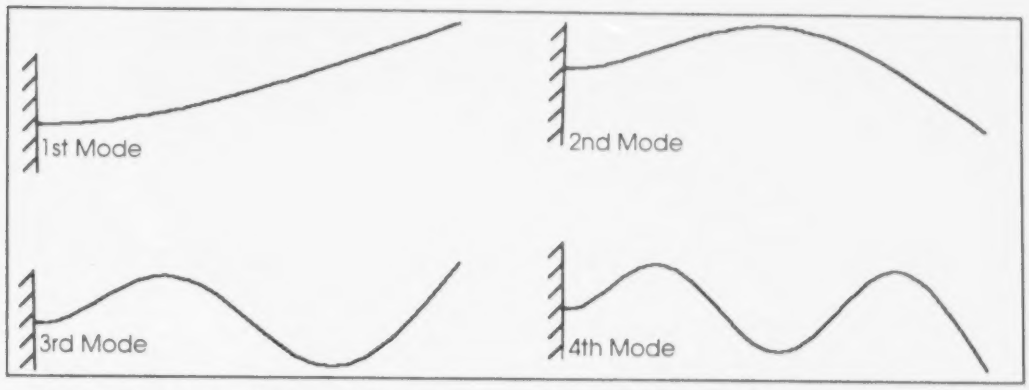

Figure 3.1: Mode Shapes of First Four Vibrational Modes of a Rectangular Cantilever

The natural resonant frequencies of the cantilever are given by Eq. (3.6). For a silicon dioxide cantilever with a rectangular cross section

$$\omega_n \propto \frac{h}{L^2} \text{ , and } \omega_1 = 5.5387 \times 10^9 \frac{h}{L^2} \text{ rad / sec, with } h \text{ and } L \text{ in } \mu\text{m}$$

assuming the density of silicon dioxide to be 2.25 g/cm^3 and Young's modulus to be 0.67×10^{12} dyn / cm^2 [3.4]. The range of frequencies for which the response of the cantilever has little or no frequency dependence is called the useful bandwidth. The useful bandwidth for a cantilever accelerometer is approximately one fifth the first resonant frequency [3.6]. Thus, a rectangular, silicon dioxide cantilever with dimensions 5 x 5 x 500 microns has a first resonant frequency of 17.63 kHz and a useful bandwidth of approximately 3.5 kHz.

Eq. (3.2), the equation of motion of the cantilever, neglects the effects of damping on the cantilever's motion. Damping can be included in the analysis by adding a generalized damping term for each mode to the time-dependent differential equation resulting from the separation of variables. This equation can then be solved using Laplace transforms. If the base of the cantilever experiences a step function acceleration then the solution is the same as that given above with the time-dependent variable, $T_n(t)$, replaced by the following:

$$T_n(t) = \frac{c_n}{b_n}[\frac{\omega_n}{\omega_d} e^{-\xi_n \omega_n t} \sin(\omega_d t + \varphi_n) - 1],$$

where, ξ_n is the Damping ratio of the nth mode, and the damped frequency of the nth mode is $\omega_d = \omega_n \sqrt{1-\xi^2_n}$; $\xi_n < 1$. Additionally, the phase angle φ_n is given by $\varphi_n = \cos^{-1}(\xi_n)$; $\xi_n < 1$, with $\alpha_n, \beta_n, c_n, b_n, \omega_n$ as given above.

Fig. 3.2 is a plot of the deflection of a cantilever's tip versus time for the first four modes of vibration, assuming a damping ratio of ξ_n = 0.05 in each mode. As can be seen in the figure, the amplitude of the deflection decreases rapidly with increasing mode number and Eq. 3.4 is therefore well approximated by summing over only the first few modes.

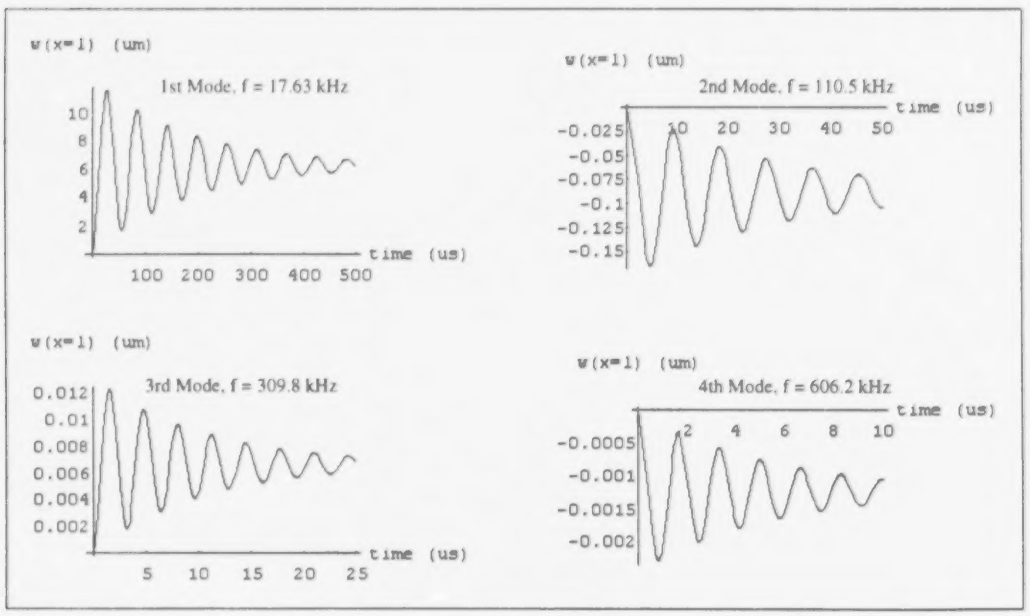

Figure 3.2 Step Response of Cantilever's Tip Due to a 5000 G Acceleration (Cantilever Dimensions 5 x 5 x 500 μm)

Fig. 3.3 shows the effect of various damping ratios on the step response of a cantilever.

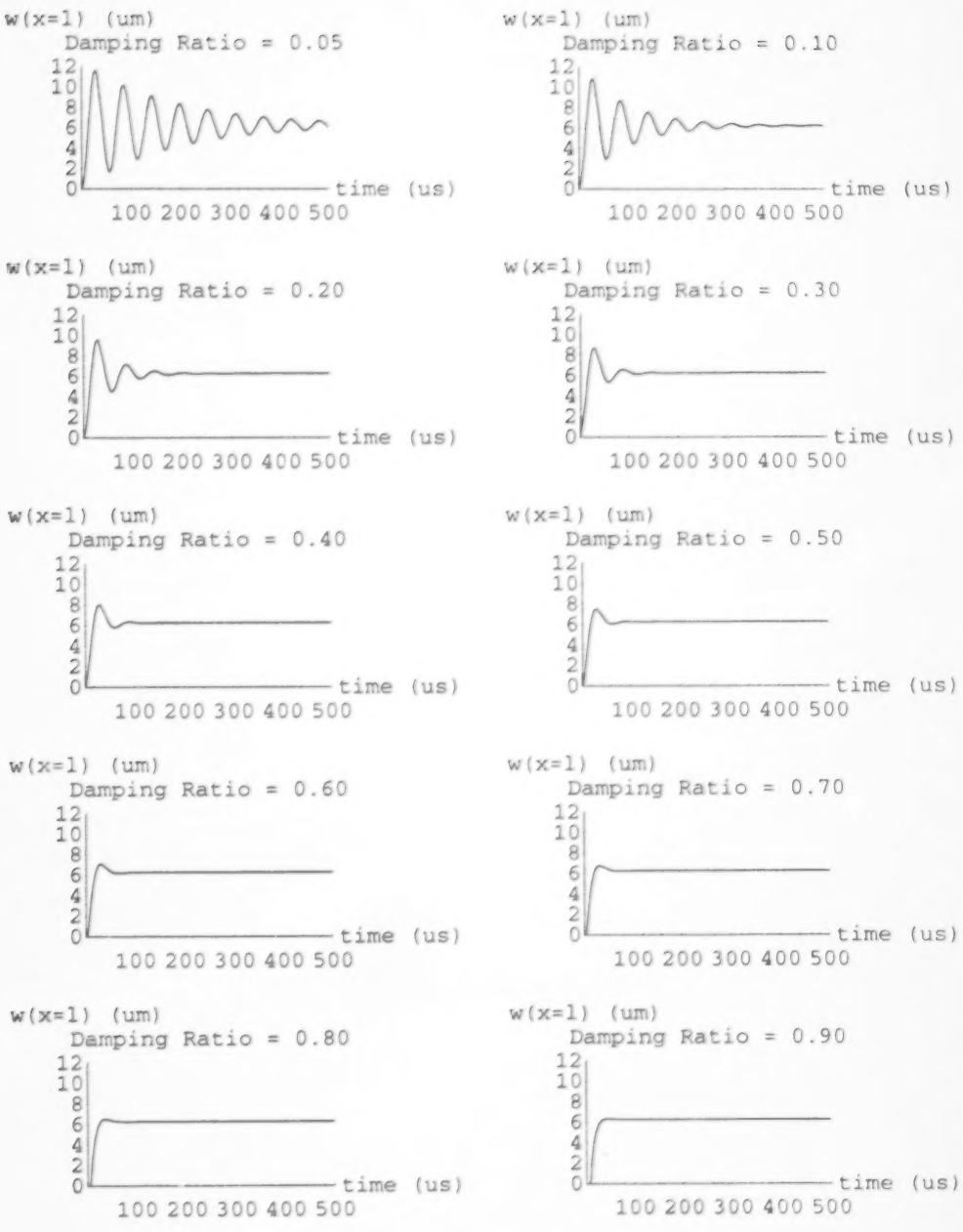

Figure 3.3: Step Response of a 5 x 5 x 500 μm Cantilever to a 5000 G Acceleration For a Range of Damping Ratios (Sum of first four modes.)

As the damping ratio is increased, the magnitudes of the resonant frequencies decrease by the factor $\sqrt{1-\xi^2_n}$, for $\xi_n < 1$. In addition, the damping results in a phase delay of $\varphi_n = \cos^{-1}(\xi_n)$, for $\xi_n < 1$. A damping ratio between 0.6 and 0.7 results in the fastest response of the cantilever and an almost total elimination of the ringing.

Damping of the cantilever results from a combination of two effects: material damping and viscous damping. Material damping is a result of a fraction of the cantilever's energy being converted to heat as the majority of the energy is transferred back and forth between kinetic and potential energy. The amount of material damping varies among different materials and is difficult to calculate accurately from material parameters. For SiO_2, material damping is expected to be small. Viscous damping is a result of viscous drag on the cantilever as it moves through the medium surrounding it. The contribution of viscous damping to the total damping of the cantilever increases with increasing viscosity of the surrounding medium. The amount of viscous damping is also dependent on the size and shape of the cavity surrounding the cantilever. The contribution of viscous damping, for a given cavity design and medium, is also difficult to model accurately.

The most accurate method of determining the total damping ratio for a given design is to measure it by measuring the exponential decay curve of the cantilever's step response. The viscosity of the surrounding medium can be controlled by varying the pressure of the gas in the cavity or by filling the cavity with a fluid. By testing various cavity designs and surrounding mediums it should be possible to achieve optimum damping of the cantilever. If, however, a fluid is used to damp the cantilever, then the sensitivity of the cantilever will be reduced due to the buoyancy forces acting on the cantilever. This can be accounted for in the analytic model by using an effective density for the cantilever equal to the density of SiO_2 minus the density of the fluid.

The above approach to the solution of Eq. (3.3) can be applied to any excitation of the base. For example, for a finite impulse acceleration of the base, the solution is as given above with the time-dependent variable replaced by [3.7]

$$T_n(t) = \frac{c_n}{b_n}\{[\frac{\omega_n}{\omega_d}e^{-\xi n\omega nt}\sin(\omega_d t + \varphi_n) - 1]u(t) - [\frac{\omega_n}{\omega_d}e^{-\xi n\omega n(t-t1)}\sin[\omega_d(t-t1) + \varphi_n] - 1]u(t-t1)\},$$

where $t1$ is the duration of the impulse and $u(t)$ is the unit step function.

Similarly, for a sinusoidal acceleration of the base, i.e. $\frac{d^2 w_b(t)}{dt^2} = a\sin(\omega_f t)u(t)$, the time-dependent variable is given by [3.7]

$$T_n(t) = \frac{c_n}{a_n}\omega_f \frac{[\frac{1}{\omega_f}\sin(\omega_f t + \varphi_{1n}) + \frac{1}{\omega_d} e^{-\xi_n \omega_n t}\sin(\omega_d t + \varphi_n)]}{\sqrt{\{4(\xi_n\omega_n\omega_f)^2 + [(\xi_n\omega_n)^2 + \omega_d{}^2 - \omega_f{}^2]^2\}}},$$

where $\varphi_{1n} \equiv \tan^{-1}\frac{-2\xi_n\omega_n\omega_f}{(\xi_n\omega_n)^2 + \omega_d{}^2 - \omega_f{}^2}$ and $\varphi_{2n} \equiv \tan^{-1}\frac{-2\xi_n\omega_n\omega_d}{(\xi_n\omega_n)^2 - \omega_d{}^2 + \omega_f{}^2}$.

3.2 Accuracy of Model

As a check on the accuracy of the model presented above, a finite element model was developed using the software package ANSYS. The ANSYS model used an 8 node, three dimensional brick element (STIF 45) and a five hundred element mesh. Also, the same boundary conditions as the model described in Sec. 3.1 were used at the fixed end of the cantilever. The ANSYS model does not neglect the effects of shear deflection or rotatory inertia and therefore is expected to be valid over a wider range of conditions. The steady state displacement versus acceleration of the cantilever tip varied on average less than 0.04% between the models. The deviation between the models increased as the beam length was decreased. The maximum difference in the results obtained using the two models was 0.15% and occurred at the minimum length tested, 100 μm.

The boundary conditions of zero displacement and slope at the fixed end of the cantilever are not strictly valid for the proposed device. A more accurate model allows for a non-zero slope and a non-zero displacement at the fixed end of the cantilever and instead uses the boundary condition of zero slope and displacement of the base of the device. This correction, however, has little effect on the displacement of the cantilever's tip. Results obtained with an ANSYS model using this boundary condition deviate less than 2% from the results obtained with the first two models.

3.3 Cantilever Design

The thickness of the cantilever was set by waveguide design considerations as discussed in Ch. 2. Fig. 3.4 shows a cross section of the cantilever waveguide. The deflection of the cantilever's tip due to a step acceleration of the base in the y-direction is independent of the cantilever's width. However, the width of the cantilever can be used to control the cross axis sensitivity of the device. The deflection of the tip of a rectangular cantilever varies inversely with the square of its thickness. If the cantilever cross section is approximated as rectangular then a 10:1 width to thickness ratio will

result in a 100:1 cross axis sensitivity ratio. With the thickness of the cantilever fixed, the length of the cantilever would be set by the acceleration range of interest.

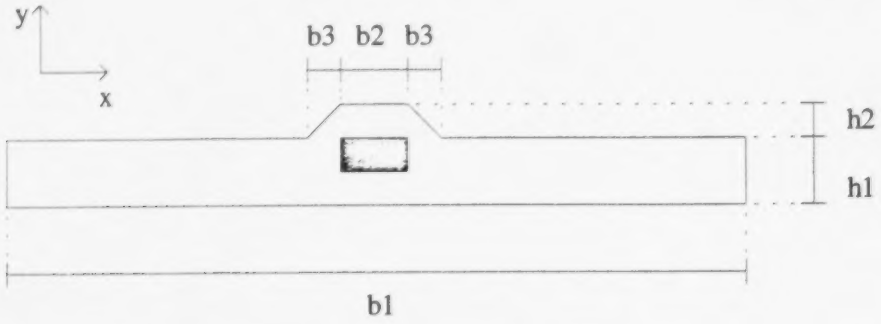

h1 = 7 μm (lower cladding layer thickness + core thickness)
h2 = 3 μm (upper cladding layer thickness)
b1 = 80 μm
b2 = 5 μm (core width)
b3 = 3 μm

Figure 3.4 Cross Section of Cantilever Waveguide

The tip deflection versus acceleration of a cantilever with this design has been plotted for a variety of lengths in Fig. 3.5. The useful dynamic range of a device with this design depends on the width of the gap at the end of the cantilever and the amount of noise in the signal. Increasing the gap results in an increase in the dynamic range of the device at the expense of measurement accuracy.

The accuracy with which the models presented in this chapter will predict the behavior of the actual device depend in part on the accuracy of the values of the material parameters used. The device was made from a ridge of phosphorous-doped SiO_2 surrounded by two layers of undoped SiO_2. All three layers were grown using plasma enhanced chemical vapor deposition. The density and Young's modulus of silicon dioxide films have been shown to depend on the process used to grow the film [3.4]. In addition, the values of these parameters are expected to change if the film is annealed. Values of Young's modulus ranging from 0.57×10^{12} dyn/cm^2 for wet thermal SiO_2 to 0.92×10^{12} dyn/cm^2 for sputtered SiO_2 have been reported in the literature [3.4]. In this analysis, Young's modulus was assumed to be 0.67×10^{12} dyn/cm^2, the value reported by Petersen [3.4] for dry thermal SiO_2. The density was also assumed to be equal to the value also reported by Petersen for dry thermal SiO_2, $\rho = 2.25$ g/cm^3. The value of Poisson's Ratio used in the ANSYS model was the value reported by Jaccodine [3.5] for

thermal SiO_2, $\nu = 0.18$. The phosphorus doping in the center layer of the cantilever was assumed to have a negligible effect on these parameters.

A)

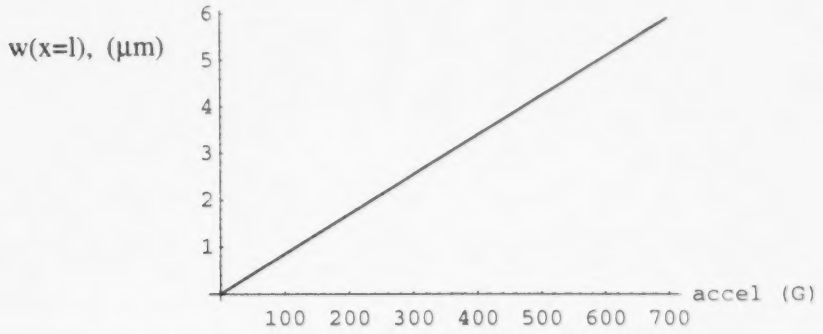

B)

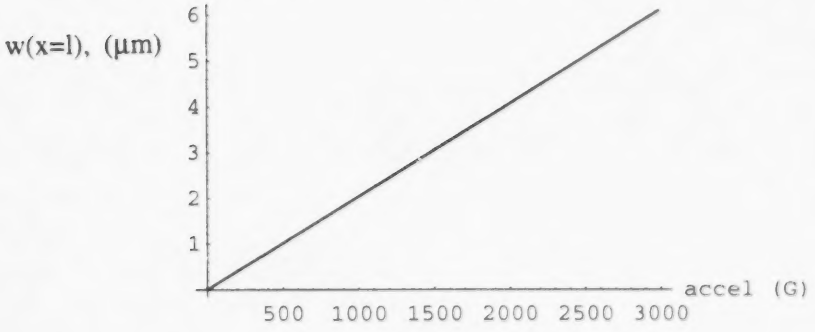

C)

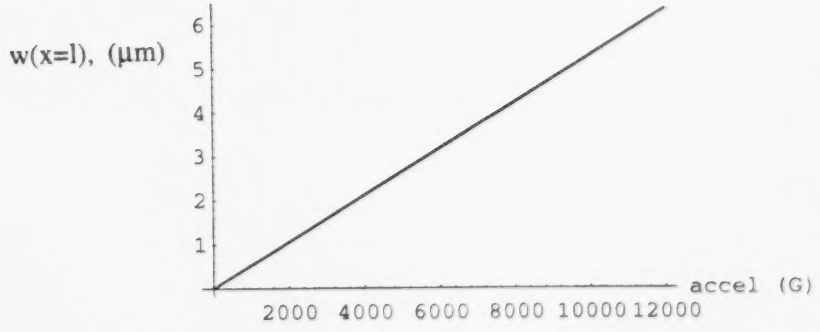

Figure 3.5 Tip Deflection versus Acceleration for a :
A) 1000 μm Cantilever, B) 700 μm Cantilever, C) 500 μm Cantilever

4 FABRICATION AND PROCESSING

Sec. 4.0, below, is a summary of the processing steps used in the fabrication of the optical accelerometer. The sections following, 4.1 to 4.15 , discuss these steps in detail.

4.0 Processing Summary

1. Deposit lower cladding layer: 4.0 microns of silicon dioxide, on a (100) silicon wafer.

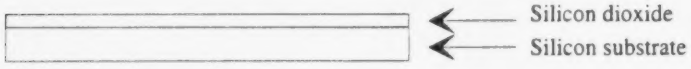

2. Deposit core layer: 3.0 microns of phosphorous doped silicon dioxide. (Phosphosilicate glass or PSG)

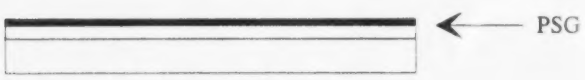

3. Cantilever maskphotolithography.

a. Spin on photoresist, soft bake, and expose.

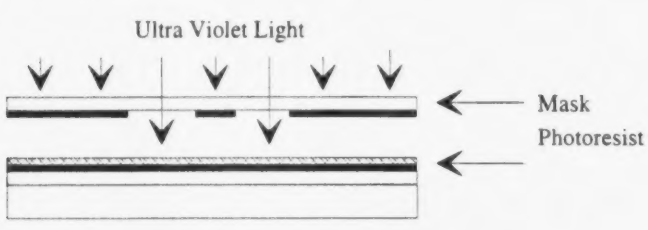

b. Develop photoresist and hard bake.

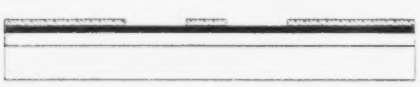

4. Reactive ion etch to form cantilever in SiO2 and PSG.

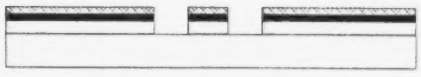

cross section side view

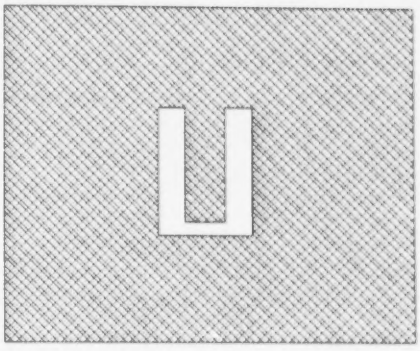

top view

5. Strip photoresist mask and remove any deposited flourocarbons or other contaminants.

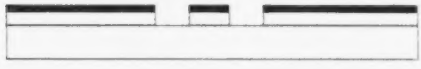

6. Waveguide core photolithography.

a. Spin on photoresist, soft bake, and expose.

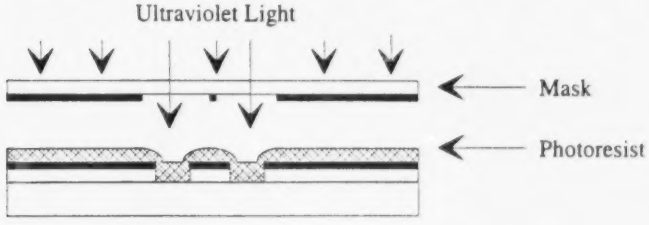

b. Develop photoresist and hard bake.

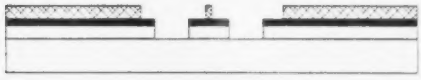

7. Reactive ion etch to form waveguide core.

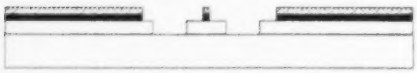

side view

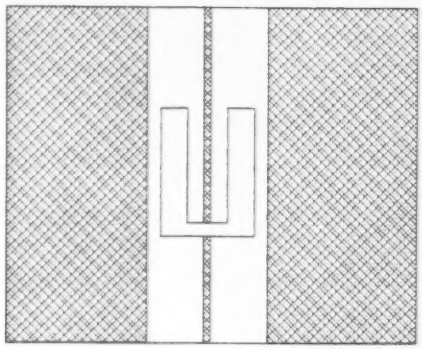

top view

8. Strip photoresist mask and remove any deposited flourocarbons or other contaminants.

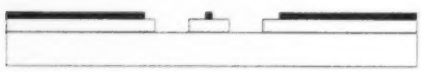

9. Anneal at 1115 degrees Celcius for 30 minutes to allow the waveguide core to flow and to densify the lower cladding layer.

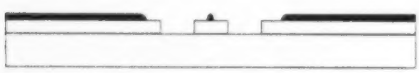

10. Deposit 0.5 microns of SiN on the bottom of the wafer to prevent the exposed silicon from being etched in the following step.

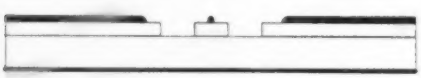

Silicon Nitride

11. Etch in ethylene diamine pyrocatacol (EDP) for 4 hours to undercut cantilevers

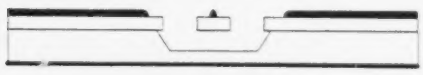

12. Deposit upper cladding layer: 3.0 microns of silicon dioxide .

13. Anneal wafer at 1115 degrees Celsius for 30 minutes in nitrogen to densify upper cladding layer and relieve stress in cantilever.

14. Coat cantilevers in photoresist for protection during the wafer dicing step.

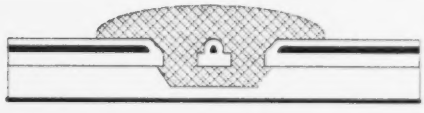

15. Dice wafer and strip photoresist.

4.1 Deposition of Lower Cladding Layer

A 4 μm layer of silicon dioxide (SiO_2) was deposited on a 3 inch (100) silicon wafer using plasma enhanced chemical vapor deposition (PECVD). The deposition was done in a Plasma Therm parallel plate reactor operating at 13.56 MHz with a lower electrode that can accommodate four three inch wafers per deposition.

The SiO_2 was deposited by the reaction of SiH_4 with N_2O in an atmosphere of He and N_2. The gas flow rates, chamber pressure, substrate temperature, input power and deposition time are controlled parameters in the deposition process. Variations in these parameters result in variations in the composition, deposition rate, refractive index, stress, and density of the SiO_2 film deposited.

The process parameters used for the SiO_2 deposition were:

5.5 sccm of SiH_4,	28 W RF Power,
600 sccm of He,	1000 mTorr,
500 sccm of N_2O,	350 °C,
100 sccm of N_2,	100 minutes.

This process resulted in an average deposition rate of 393 Å/min and an average refractive index of 1.464, measured by ellipsometry immediately after the deposition. The average variation in thickness across a wafer was 0.2% and the average deviation in the deposition rate between runs was 1.7%. The average deviation in the refractive index across the wafer was 0.02%, and the average run-to-run variation in refractive index was 0.04%.

The refractive index of the SiO_2 deposited using this process was not constant with time. On average it increased to a value of 1.467, over a period of a few hours after the deposition. The refractive index could be temporarily reduced to its original value by vacuum baking the film at 110 °C for five minutes, indicating that the rise is probably due to water absorption. The temporal drift in the index of the films was permanently removed by annealing them at 1115 °C in dry nitrogen for half an hour. Refer to Sec. 4.9 for details of the procedure. After the anneal, the refractive index decreased to an average value of 1.456 and the thickness of the film was reduced by an average of 4%.

The deposition rate can be increased by increasing the input power and/or by increasing the silane flow rate. These changes, however, result in less dense films with less uniform thickness and refractive index variations across the wafer. Decreasing the flow rates of the dilution gases, He and N_2O, also tends to decrease the uniformity of the refractive index and the thickness of the film. Decreasing the substrate temperature tends to decrease the film stress as well as the film density.

4.2 Deposition of Core Layer

A three micron layer of phosphorus-doped silicon dioxide was deposited on top of the lower cladding layer using PECVD. The process used was similar to the process described in Sec. 4.1, except for the addition of phosphine (PH_3) to the gas mix. The phosphine addition results in the incorporation of phosphorus into the SiO_2 film and an increase in the refractive index. The refractive index of SiO_2 increases linearly with the molar concentration of P_2O_5 in the film [4.1]. The amount of phosphorus doping in the film can be controlled by varying the ratio of SiH_4 to PH_3 flow [4.2]. Fig. 4.1 shows the relation between average refractive index and phosphine flow for the process used in this step. The refractive index was measured several hours after the deposition. The refractive index of films grown using 1.2 sccm of PH_3 dropped from the value shown in the figure over time and showed signs of sweating phosphoric acid.

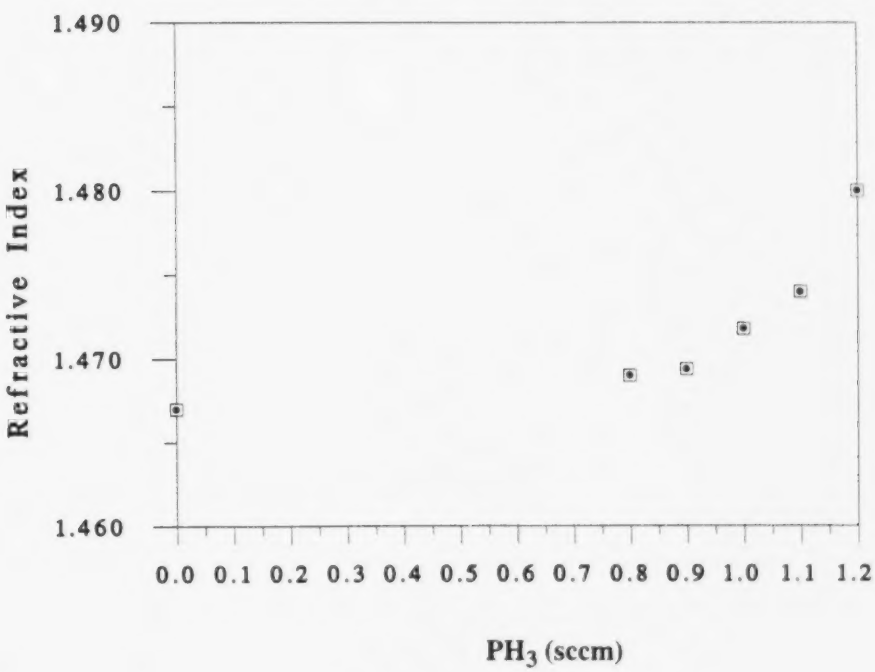

Figure 4.1 Stabilized Average Refractive Index versus Phosphine Flow (Unannealed)

In order to obtain a difference in refractive index between the core and cladding layers of 0.004, a core layer with a refractive index after annealing of 1.460 is desired. The process parameters used to attain this were:

5.5 sccm of SiH_4,	28 W RF Power,
600 sccm of He,	1000 mTorr,
500 sccm of N_2O,	350 °C,
100 sccm of N_2,	67 minutes,
0.9 sccm of PH_3.	

This process resulted in an average deposition rate of 445 Å/min and an average refractive index 1.455, measured immediately after the deposition. The average variation in thickness across a wafer was 0.4% and the run-to-run average deviation in the deposition rate was 0.3%. The average refractive index variation across the wafer was 0.04%, and the average run-to-run variation in refractive index was also 0.04%. The increase in the average deviation in thickness and refractive index, as compared to the undoped SiO_2, was probably due to variations in the flow rate of PH_3. In this process, the mass flow controller used to control the delivery of PH_3 was operated near the lower end of its controllability. The average deviation in the thickness and refractive index would probably be improved with better control of the PH_3 delivery.

Several hours after the deposition, the refractive index of the films grown using this process increased to an average value of 1.469. The refractive index of these films could be temporarily reduced to an average value 1.462 by vacuum baking the film at 110 °C for 5 min. This index value is significantly larger than the value measured immediately after the deposition, indicating that the rise in index was probably due to both water absorption and to a chemical change in the film. The temporal drift in the index of the films was permanently removed by annealing them at 1115 °C in dry nitrogen for half an hour. Refer to Sec. 4.9 for details of this process. After the anneal the refractive index decreased to an average value of 1.460 and the thickness of the film was reduced by an average of 4%.

4.3 Photolithography

Standard Alberta Microelectronics Centre (AMC) photolithographic processes were used to transfer the mask pattern to the photoresist spun onto the wafer. The photolithographic recipe used in this step is summarized in Sec. 4.3.1 below. The process used for this step deviates from the standard AMC lithographic process in the final hard bake step. The standard 50 second vacuum hard bake was replaced with a 30 minute,

140°C convection hard bake. The higher temperature, longer duration hard bake makes the resist more resilient and also causes the photoresist to reflow. The reflow helps to partially smooth out roughness in the transferred pattern. The hard baked photoresist loses its resilience with time, making it important to minimize the time between hard baking and the following reactive ion etching step.

4.3.1 Standard Photolithographic Process

1. Coat wafer with hexamethyldisilazane (HMDS) to improve photoresist adhesion.
2. Spin on 3 mL of HPR 504 positive photoresist: 500 rpm, 5 second spread cycle, 3500 rpm, 15 second spin cycle.
3. Vacuum soft bake at 110 °C for 50 seconds.
4. Align mask alignment lines parallel to wafer flat and expose for 2.8 seconds.
5. Hand develop in HPR 352 positive photoresist developer for 20 seconds.
6. Hard bake at 140 °C for 30 minutes.

4.4 Reactive Ion Etching

A Plasma Therm Batch Top reactive ion etching (RIE) system was used to etch the cantilever pattern in the doped and undoped SiO_2 layer as illustrated in Fig. 4.2. The system utilizes an RF power source operating at 13.56 MHz to generate a plasma in a low pressure gas. Three process gases were available: CF_4, CHF_3 and O_2. Within the plasma, free radicals, ions and electrons are generated from the gas species. There are two basic etch mechanisms in reactive ion etching: chemical etching and sputter etching.

Chemical etching is the result of free radicals generated in the plasma reacting with the material to be etched to form volatile reaction products. These reaction products are then pumped out of the chamber. For example, in the etching of silicon in a CF_4 plasma, free fluorine combines with the silicon to form SiF_4:

$$Si_{(s)} + 4F_{(g)} \text{----> } SiF_{4(g)}.$$

Chemical etching is isotropic, resulting in a rounded sidewall profile. If the reaction product is nonvolatile, such as occurs in the reaction of aluminum with free fluorine, the surface to be etched becomes passivated with the nonvolatile reaction product and no further etching occurs.

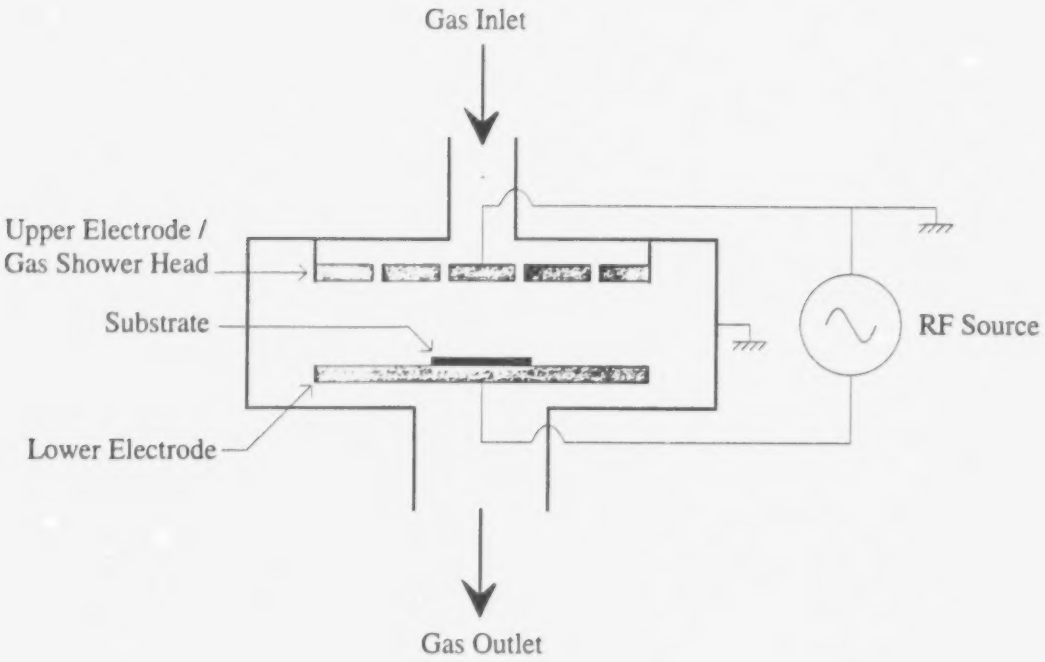

Figure 4.2 Reactive Ion Etching System

Sputter etching results because of the potential generated between the lower electrode and the plasma. This bias accelerates the ions generated in the plasma towards the substrate on the lower electrode, resulting in the bombardment of the substrate surface. If the ions attain sufficient energy, they can remove substrate material upon impact with its surface. Unfortunately, the ion bombardment can also result in the sputter etching of the mask. The etch rate due to sputtering is highly dependent on the voltage potential between the plasma and the lower electrode and results in an anisotropic etch profile.

In the reactive ion etching of many materials, the two etch mechanisms described above combine synergistically, resulting in an etch rate which exceeds the sum of the individual etch mechanisms. This effect is due to an increased reactivity in the substrate surface, resulting from the impact of ions with insufficient energy to dislodge substrate

The flow rate of the process gases, the chamber pressure and the input power are controlled variables in the etching process. The values of these parameters affect the etch rate and the anisotropy of the sidewall profile.

A pure CHF_3 etch process was used for this step because a large etch selectivity can be achieved between SiO_2 and silicon using this gas. In addition, the etch rate of the photoresist mask was found to be much lower in a CHF_3 plasma then in a CF_4 plasma. When CHF_3 is used, a fluorocarbon film is deposited throughout the chamber during the etch process. This film is more readily etched on SiO_2 than on silicon resulting in an etch selectivity between the two materials [4.3]. As the fluorocarbon film builds up in the chamber, the voltage bias begins to drop, decreasing the etch rate. In order to make the process repeatable, it is necessary to clean the chamber prior to the etch using a high power and high pressure O_2 plasma.

The process parameters used to etch the cantilevers were:

40 sccm CHF_3,	100 W RF,
40 mTorr,	120 min.

This process results in an average etch rate of 280 Å/min. and a side wall profile of approximately 85 degrees. The etch rate was found to be very nonuniform across the RIE chamber. In order to maximize the uniformity of the etch across the wafer, it is important to ensure that the wafer is placed in the center of the chamber and does not drift from this position while the chamber is pumped out. This can be achieved by placing two small glass slides on the edge of the wafer, pinning it down. Even with this precaution, the edges of the wafer etch between 10% and 40% faster than the center of the wafer. No means of end point detection was available, so a timed etch was used. The nonuniformity in the etch rate is not critical in this step as long as the etch is timed using the etch rate at the center of the wafer. In order to ensure completion of the etch, a 10% over-etch was used.

4.5 Mask Strip and Wafer Clean

The majority of the photoresist mask was removed by placing the wafer in ultrasonically agitated acetone for five minutes. Any remaining photoresist or deposited fluorocarbon film was removed by placing the wafer in "Piranha" solution for twenty minutes. "Piranha" solution is an aggressive etchant composed of a three to one mixture of sulfuric acid and 30% hydrogen peroxide.

4.6 Waveguide Photolithography

The photolithographic process used in this step differs from the standard process described in Sec. 4.3 in several ways. The spin speed is reduced in order to increase the photoresist thickness. This is necessary to improve the step coverage of the photoresist in the regions were the cantilevers have been etched. The rest of the process was also modified to account for the thicker layer of photoresist. The complete photolithographic recipe can be found in Sec. 4.6.1 below. Although the lower spin speed improves the step coverage, the photoresist still tends to thin in the regions where the cantilevers have been etched as seen in Fig. 4.4. This thinning can cause the mask to fail during following reactive ion etching step, resulting in nonfunctional devices. Fig. 4.3 is a scanning electron microscope (SEM) photograph of a waveguide core which was thinned in the region near the cantilever because of insufficient photoresist thickness in this region.

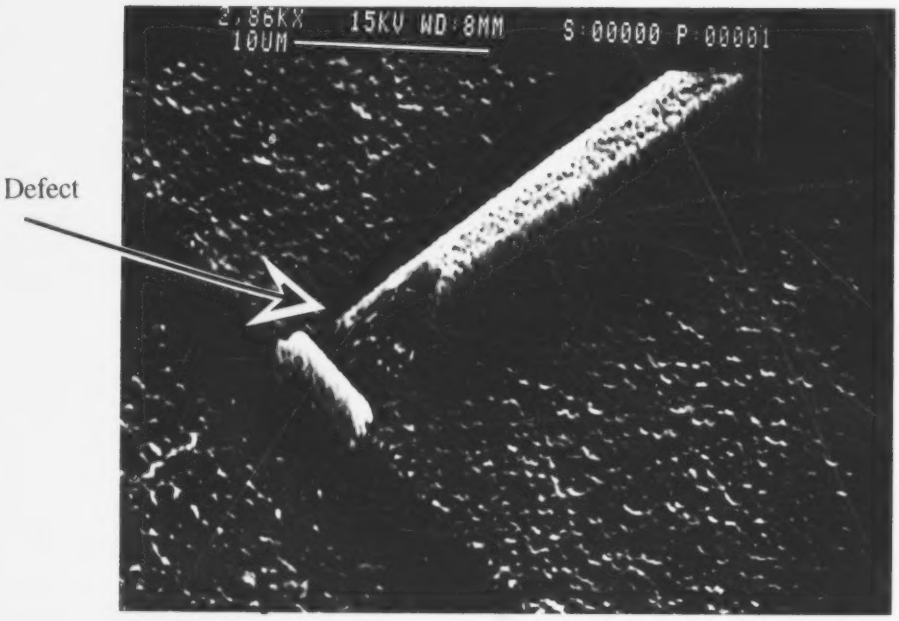

Figure 4.3 SEM photo of step coverage defect in etched waveguide core

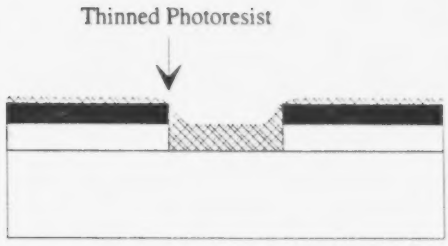

Figure 4.4 Photoresist mask thinning due to step topography

This problem could probably be alleviated by using a more viscous photoresist; however, none was available during this project.

4.6.1 Modified Photolithographic Process for Improved Step Coverage

1. Coat wafer with hexamethyldisilazane (HMDS) to improve photoresist adhesion.
2. Spin on 5 mL of HPR 504 positive photoresist: 500 rpm, 5 second spread cycle 2000 rpm, 15 second spin cycle.
3. Vacuum soft bake at 110 °C for 90 seconds.
4. Align mask alignment lines parallel to wafer flat and expose for 4.8 seconds.
5. Hand develop in HPR 352 positive developer for 40 seconds.
6. Hard bake at 140 °C for 30 minutes.

4.7 Reactive Ion Etch Waveguide Core

The parameters of the RIE process used in this step, to etch the core of the waveguide from the phosphorus-doped glass, were identical to the parameters listed in Sec. 4.4. The etch time for this step was reduced to 140 minutes. This results in approximately one micron of over-etch on the outside of the wafer and very little over-etch in the center of the wafer. Fig. 4.5 is a SEM photo of a cross section of the waveguide core showing the etch profile. The "grass" or "spikes" seen in this photo is probably caused by the heavy ion pounding resulting from the high voltage bias of this process.

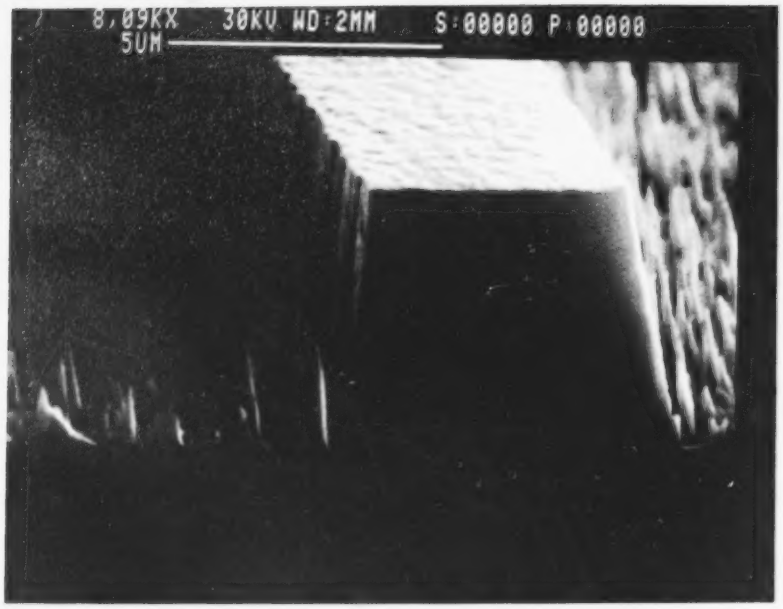

Figure 4.5 SEM Photo of the Waveguide Core Cross Section

4.8 Mask Strip

This step is identical to step 4.5. However, in this step, it is critical to remove the photoresist mask and deposited fluorocarbons completely because any contaminants left on or near the waveguide will act as scattering centers and increase the waveguide losses. In addition, any photoresist or fluorocarbons remaining on the wafer surface can impede the adhesion of the cladding layer and result in it peeling off during the following processing steps.

4.9 Flow Waveguide Core

The roughness in the sidewall profile of the waveguide core can be reduced by heating the wafer to a temperature higher than the glass transition temperature of phosphorus-doped SiO_2 and allowing it to flow. Reducing the sidewall roughness reduces scattering losses in the waveguide. The glass transition temperature of phosphorus-doped SiO_2 decreases as the concentration of phosphorus in the glass increases [4.4-4.5]. The degree of flow is dependent on the anneal time, temperature and

ambient atmosphere. Increased flow occurs with increased temperature and with increased anneal times. Introducing water vapor into the ambient atmosphere also increases the degree of flow [4.6].

In the fabrication of this device, it is necessary to anneal the glass in dry nitrogen to prevent the thermal oxidation of the exposed silicon surfaces. It is also desirable to minimize the temperature and length of the anneal for two reasons. First, increasing the length and temperature of the anneal increases the chance of bubble formation at the surface due to trapped gases escaping from the softened glass, (see Fig. 4.6). Second, diffusion of phosphorus from the core into the cladding layer increases with increasing anneal time and temperature. Phosphorus diffusion into the cladding is undesirable because it will increase the penetration of the mode field into the cladding and therefore increase the substrate leakage losses.

The process used for this step was a thirty minute anneal at 1115 °C in a flow of 3.4 L/min. of nitrogen at a pressure of 15 psi. Fig. 4.7 is a SEM photo of the core of the waveguide after it was annealed. The sidewall roughness was substantially reduced and no bubbling was observed.

In order to determine the extent of the phosphorus diffusion which occurs during the anneal, the process was simulated using the semiconductor process software simulation package SUPREM [4.10]. The results of this simulation indicate that the amount of diffusion is small and should have little effect on the mode profile of the waveguide as seen in Fig. 4.8. The default value of the diffusion constant for phosphorus in SiO_2 was used for the simulation. However, the diffusion mechanism of phosphorus in SiO_2 and thus the diffusion constant is known to depend strongly on the phosphorus concentration [4.7-4.8]. The results of the simulation should therefore only be considered as approximate.

Figure 4.6 SEM Photo of Bubble Formation due to Excessive Anneal Temperature

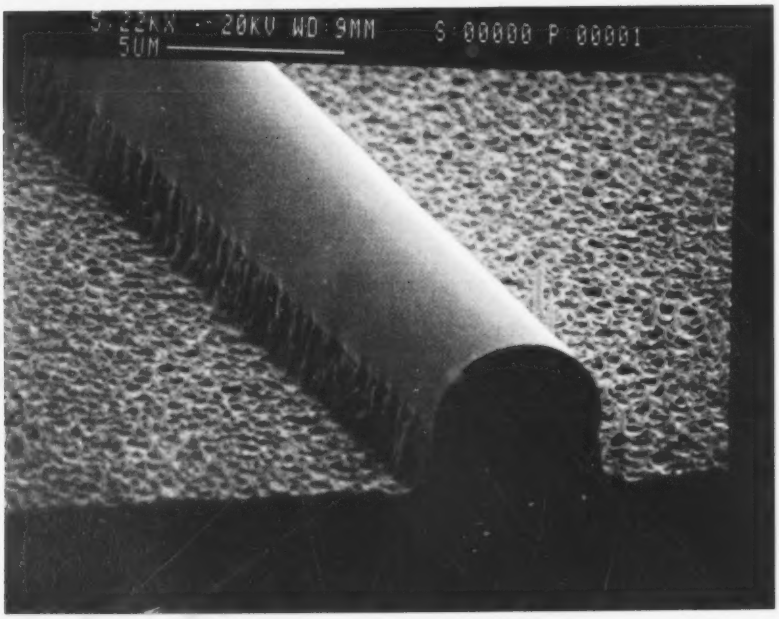

Figure 4.7 SEM Photo of Waveguide Core After Anneal

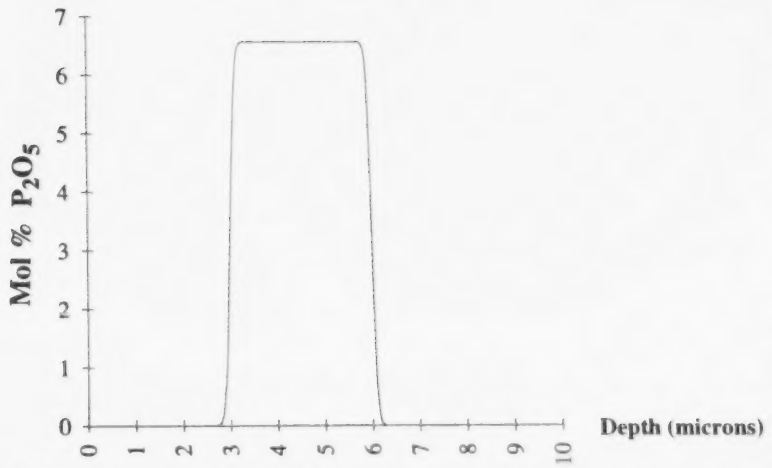

Figure 4.8 SUPREM Simulation of Phosphorus Diffusion Resulting from Anneal

4.10 Deposition of Silicon Nitride Mask

PECVD was used to deposit a 5000 Å layer of silicon nitride (SiN) onto the back of the wafer. SiN has a very low etch rate in ethylene diamine pyrocatacol (EDP) and prevents the back of the silicon wafer from being etched in the following step. The process parameters for this step can be found in Sec. 4.10.1 below.

4.10.1 SiN Deposition Process

Pressure	1000 mTorr
Temperature	350 °C
Power	55 W RF
NH_3 flow	2.5 sccm
SiH_4 flow	6.0 sccm
He flow	620 sccm
N_2 flow	280 sccm
Deposition Time	45 min.

4.11 Undercut Cantilevers in EDP

The silicon around and under the cantilevers was removed using a four hour EDP etch process. The EDP is heated to 115 °C and agitated using a magnetic stirrer. The complete process recipe for this step can be found in Sec. 4.11.1.

EDP is an anisotropic etchant of silicon. It etches single crystal silicon in the (100) direction approximately 35 times faster than in the (111) direction. The etch rate in

the (100) direction is approximately 1.25 μm/min., but varies with the age of the EDP solution and the amount of exposed silicon [4.9].

If the sides of the cantilever opening in the oxide mask are aligned with the planes of the silicon crystal, the exposed silicon will be rapidly etched until the only (111) planes are exposed. At this point, a pyramidal shaped trench formed by intersecting (111) planes has been etched under the cantilever and the etch rate is drastically reduced, as shown in Fig. 4.9.

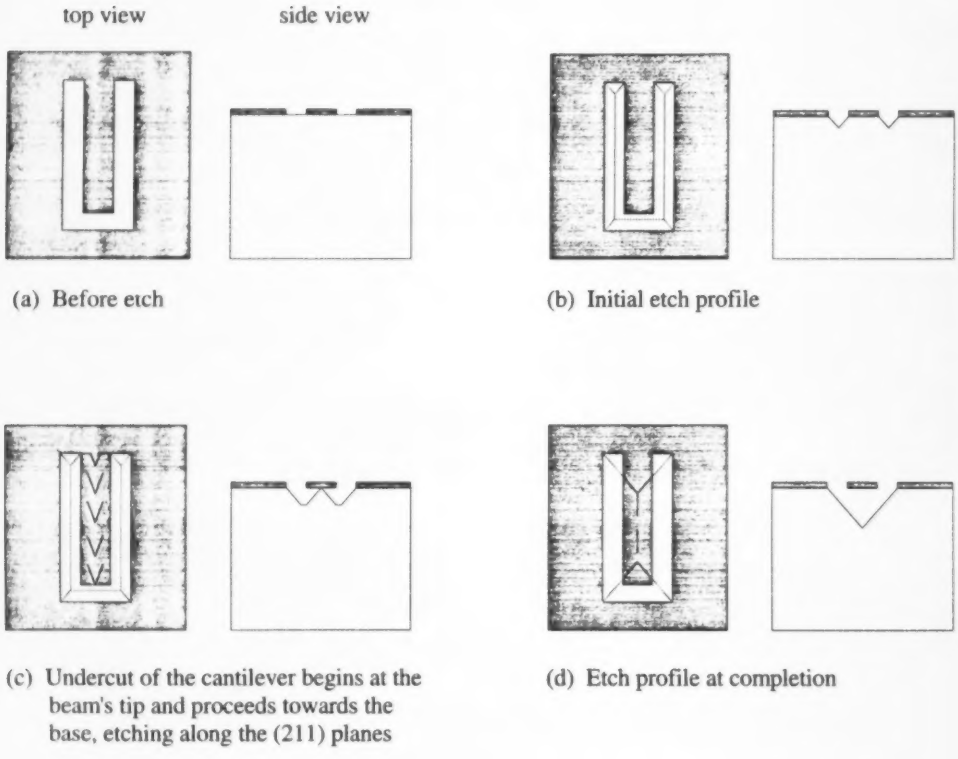
top view
side view
(a) Before etch
(b) Initial etch profile
(c) Undercut of the cantilever begins at the beam's tip and proceeds towards the base, etching along the (211) planes
(d) Etch profile at completion

Figure 4.9 Cantilever Undercut Process

Fig. 4.10 is a SEM photo of a free-standing oxide cantilever beam. The deposited SiO_2 from which the cantilever is cut is under stress. The stress arises partially from the deposition process and from thermal mismatch between the silicon substrate and the SiO_2 film. When the beam is freed from the underlying silicon, the beam bends to relieve this stress.

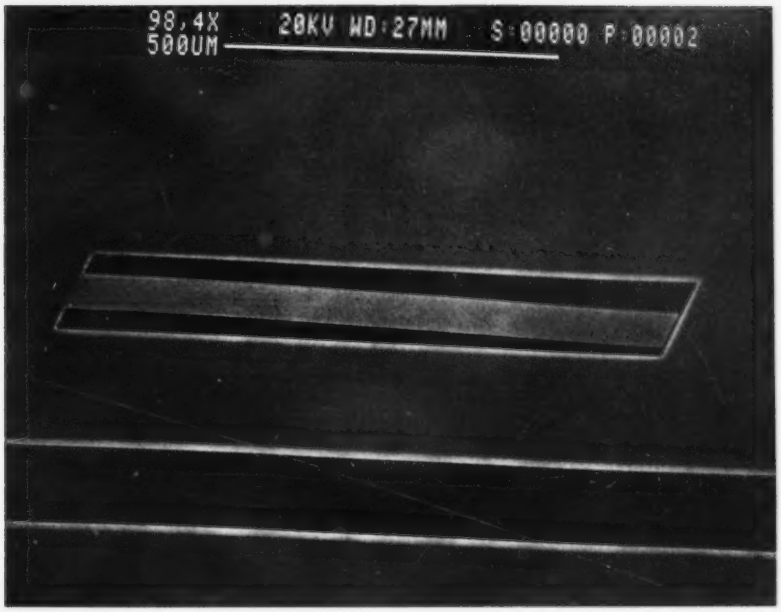

Figure 4.10 SEM Photo of Free Standing SiO_2 Cantilever Beam

EDP also etches SiO_2 at a rate of approximately 8 Å/min. The "grass" seen in Fig. 4.5 has a large surface area exposed to the EDP during this step and is virtually removed during the etch as shown in Fig. 4.11. This is beneficial because the "grass" would cause low density regions when the upper cladding layer is deposited, resulting in an increase in the scattering losses of the waveguide. The etching of the SiO_2 mask by the EDP also results in the cantilever beam being thinned. The top of the beam is exposed to the EDP for the entire duration of the etch, resulting in approximately 0.1 μm of etching. The undercutting of the cantilever proceeds from the tip of the beam towards the base. The bottom surface of the tip of the beam is therefore exposed to the EDP for the majority of the etch, resulting in it being thinned by approximately 0.1 μm. The bottom surface of the base of the beam, however, is only exposed to the EDP at the end of the etch, resulting in a tapered beam profile. This tapered beam profile was modeled using ANSYS and the deflection versus acceleration properties where found to differ by less than 2% from the untapered profile.

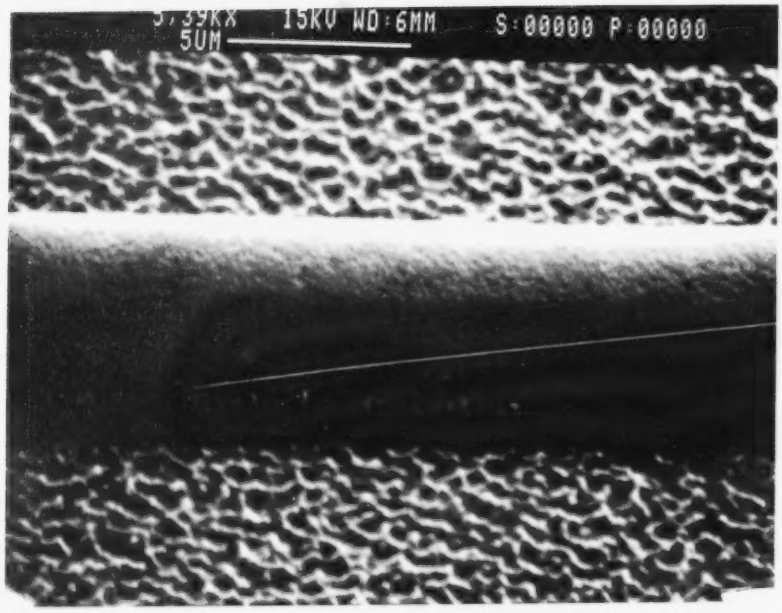

Figure 4.11 SEM Photo of Waveguide Core and Surrounding Area after EDP Etch

4.11.1 EDP Recipe

1) 10 second etch in 10:1 Buffered Oxide Etch to remove native oxide.
2) 4 hour etch in stirred, 115 °C EDP. (EDP composition: 750 mL ethylene diamine, 120 g pyrocatacol and 240 mL deionized water)

4.12 Deposition of Upper Cladding Layer

The process used for this step was identical to the process described in Sec. 4.1 with the deposition time reduced to 70 minutes.

4.13 Densification of Upper Cladding Layer

The wafer was annealed at 1115 °C for 30 minutes in dry nitrogen. The anneal densifies the SiO_2 deposited in step 4.12, lowering the scattering losses in the waveguide. The anneal also affects the stress in the cantilever. In general, the cantilever beams were bent down prior to this step. After the anneal, the downward deflection was reduced and in some cases reversed. The change in deflection varies with the length of the beams and is probably caused by stress induced by the thermal mismatch of the materials rather than

4.14 Preparation of Free Standing Cantilevers for Wafer Sawing

Photoresist was deposited onto the free standing cantilevers using an eye dropper. The photoresist was then hardened by baking it at 70 °C for half an hour. The hardened photoresist holds the cantilevers in place and reduces the chance of damage by the wafer saw cooling water during the dicing process.

4.15 Wafer Dicing

The wafer was diced, with each die containing a single cantilever. The photoresist was then stripped using acetone, isopropyl alcohol and water. Fig. 4.12 below is a SEM photo of a complete device. The upward deflection of the beam is a result of annealing at too high a temperature in step 14; however, this deflection facilitates the testing of the device as will be discussed in Sec. 5.3.

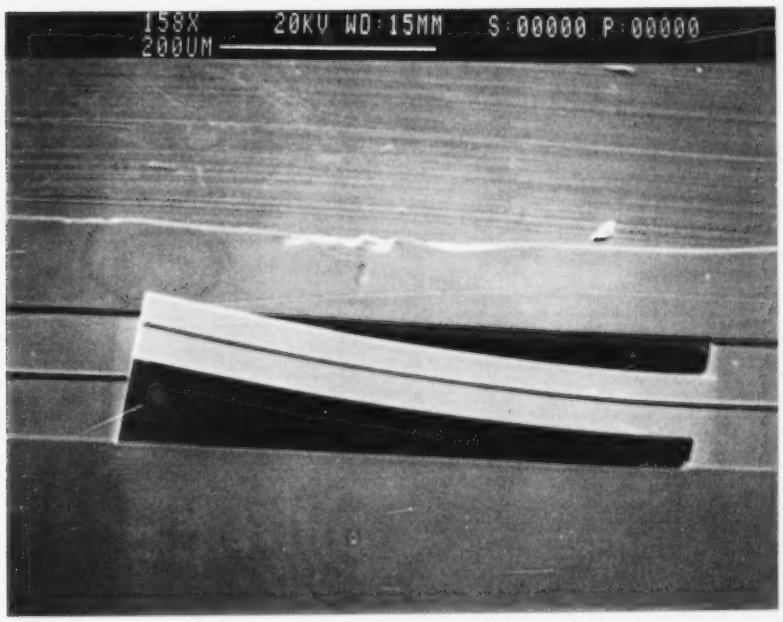

Figure 4.12 SEM Photo of Finished Device

5 TESTING

5.0 Introduction

Throughout the development of the fabrication process described in Ch. 4, several sets of waveguides and waveguide cantilevers were fabricated and tested. In this chapter, the techniques used to test these devices are described and test results for the devices fabricated using the final process are presented and discussed. The first section covers waveguide loss measurements and the second section covers imaging the near-field pattern emitted from the waveguides. The third section of this chapter covers the measurement of emitted optical power versus cantilever displacement.

The waveguides used for the measurements presented in Secs. 5.1 and 5.2 were fabricated using a slightly modified version of the process described in Ch. 4. The steps used to fabricate the free-standing cantilever (3,4,5,10,11,14 and 15) are not required in the fabrication of waveguides and were omitted. Also, a 6 minute, 50:1 buffered oxide etching step was added after step 8, to remove the grass spikes which are normally removed during the omitted EDP etching step. The waveguide cantilevers used in the displacement measurements presented in Sec. 5.3 were fabricated using the complete process described in Ch. 4.

A 675 nm semiconductor laser with a singlemode fiber pigtail delivering 1000 μW of power was used as the optical source for all measurements. The fiber pigtail was spliced to a singlemode fiber with a NA of 0.1 and a core diameter of five microns. The end of the spliced fiber was prepared by stripping the plastic jacket and cleaving the end. Similarly, the ends of the waveguide were prepared by cleaving the wafer perpendicular to the waveguide. Light was coupled into the waveguide by butt-coupling the source fiber to the cleaved end of the waveguide. The fiber was aligned with the waveguide under a microscope using piezoelectric micropositioners while the power emitted from the waveguide was monitored. The source was considered to be aligned when the power coupled out of the waveguide was maximized.

5.1 Waveguide Loss Measurements

Figure 5.1 depicts the experimental setup used to measure the waveguide loss properties. Light scattered from the top surface of the waveguide was gathered using a plastic multimode fiber with a NA of 0.5. The ends of the plastic pickup fiber were prepared by polishing them with a water-lubricated 1-μm-grit polishing paper. The

intensity of the gathered light was measured using a silicon photodetector connected to a NEWPORT optical power meter. The pickup fiber was aligned with the waveguide and scanned along its length using an xyz micropositioner. The center of the pickup fiber was aligned approximately 1 mm above the center of the waveguide and its lateral and vertical position, relative to the central axis of the waveguide, was maintained constant as it was scanned along the length of the guide. The measurements were made in a darkened room in order to reduce noise from ambient light. In addition, light from the source fiber which was not coupled into the waveguide was prevented from skimming along the surface and adding noise to the desired signal by placing a small plastic block on top of the waveguide, immediately after the source fiber.

The scattered light intensity was recorded at 0.5 mm intervals along an 18.5 mm section of the waveguide and plotted versus distance on a log scale. The slope of this graph gives the waveguide loss in dB/cm. This approach to loss measurement is based on the assumptions that scattering centers are of equal size and uniformly distributed along the waveguide. The power propagating in the guide is therefore assumed to be proportional to the scattered light intensity and the waveguide loss is assumed to be equal to the change in scattered light intensity with distance.

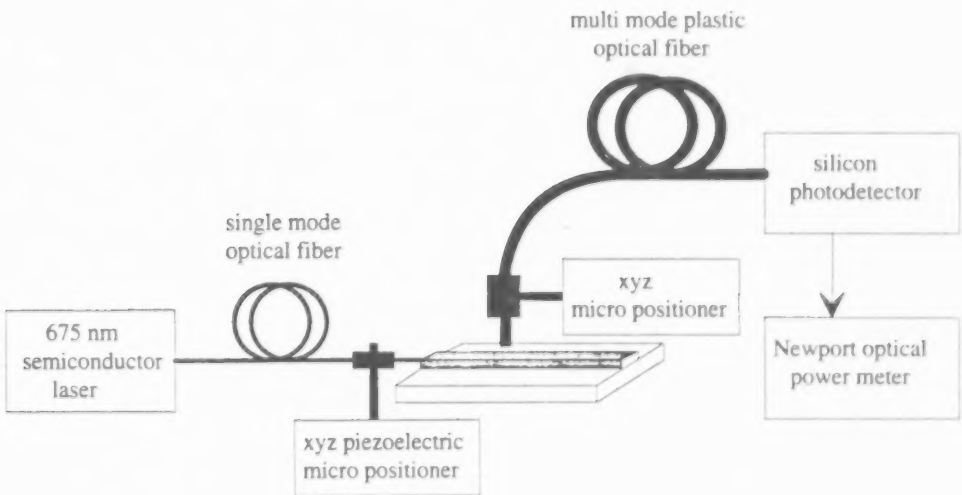

Figure 5.1 Waveguide Loss Measurement Setup

Loss measurements were made on the waveguides at three stages during their fabrication: 1) prior to the deposition of the upper cladding layer, 2) immediately after the deposition of the upper cladding layer, before densification, and 3) after the final upper cladding densification step. Typical loss curves for the first two types of waveguides are shown in Figs. 5.2 and 5.3. The average loss of the first class of waveguides was found to be 1.1 dB/cm. This loss is probably predominantly due to a combination of substrate leakage and scattering from dust particles on the surface of the core. The average loss for the second type of waveguide was 3.4 dB/cm and the average power coupled out of the guide was 5 μW. The mode profile of a waveguide without an upper cladding layer is not symmetric about the center of the waveguide but shifted towards the substrate. With the addition of the upper cladding, the waveguide mode profile becomes symmetric and shifts away from the substrate. The losses due to substrate leakage should therefore be reduced after the upper cladding layer is added. Thus, the increase in loss which was observed is most likely caused by an increase in scattering due to low density regions in the upper cladding layer. Loss measurements of the third class of waveguides were inconclusive. Plots of the scattered light intensity versus distance did not have well-defined slopes. The average power coupled out of the waveguide, however, increased to 95 μW after the final densification step. Using the loss, length and average output power measured for the second class of waveguide, the average power coupled into the waveguides was calculated to be 115 μW. Assuming the same average optical power was coupled into the guides after annealing, the average loss of the third class of waveguides was calculated to be 0.2 dB/cm. The reduction in loss is likely a result of a reduction in scattering losses due to an increase in the uniformity of the upper cladding layer.

The estimated average loss of 0.2 dB/cm that was achieved after the final processing step is comparable to the loss values ranging from 0.01 dB/cm to 6 dB/cm which have been reported in the literature for a variety of waveguide designs [5.1 - 5.8]. In addition, input coupling and waveguide losses as low as 7 dB were achieved for a 4 cm section of waveguide indicating that good coupling between the source fiber and waveguide was also achieved.

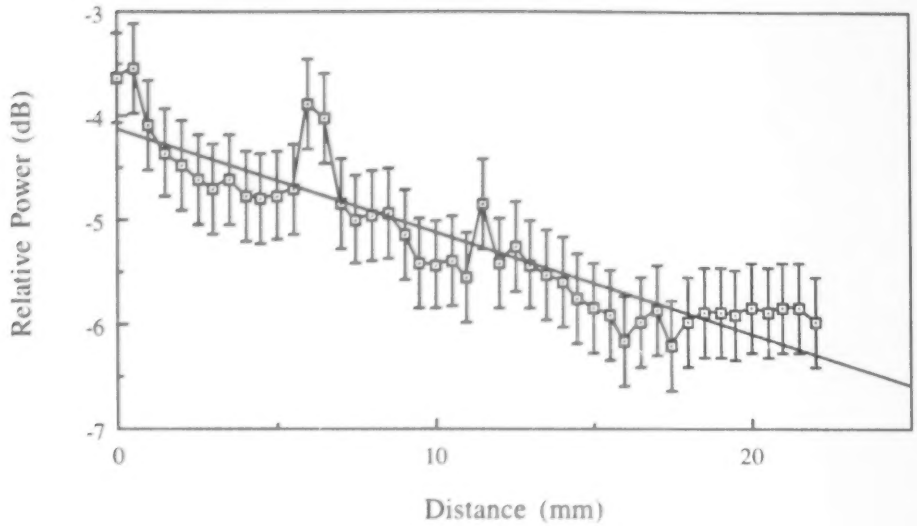

Figure 5.2 Typical Scattered Light Intensity versus Distance Plot for an Unclad Waveguide. Loss = 0.98 dB/cm
Least Squares Curve Fit: $y = -4.1325 - 0.097906x$, $R^2 = 0.822$

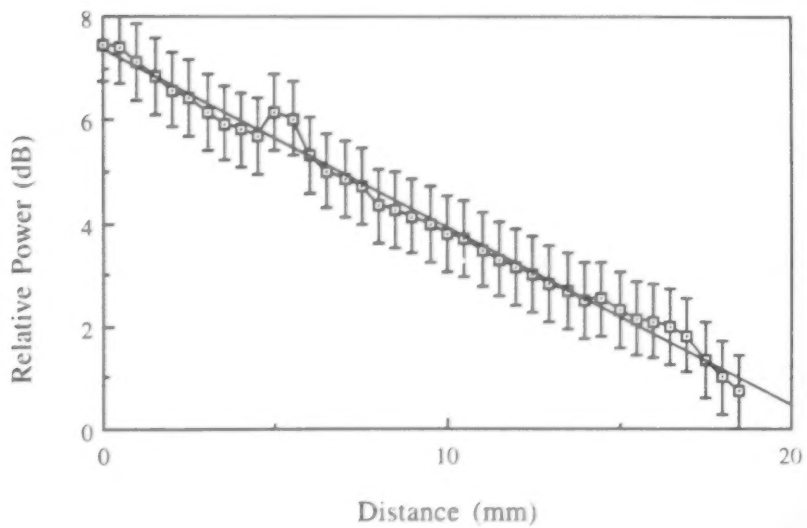

Figure 5.3 Typical Scattered Light Intensity versus Distance Plot for a Clad Waveguide before Annealing. Loss = 3.4 dB/cm.
Least Squares Curve Fit: $y = 7.3507 - 0.34336x$, $R^2 = 0.990$

Although the waveguide loss achieved with this process is adequate for the application, the loss could be further reduced in two ways. First, substrate leakage losses could be reduced by increasing the thickness of the lower cladding layer. In this application, however, an increase in the thickness of the lower cladding layer will result in an increase in the stiffness of the cantilever beam and a subsequent decrease in the device's sensitivity for a fixed beam length. Second, the losses due to scattering could be decreased by reducing the exposure of the core to dust particles. The majority of the processing steps used in the fabrication of the waveguides were done in a clean room environment; however, the two annealing steps were not. The wafers were therefore exposed to higher levels of dust and contaminants during these two processing steps then during the rest of the process. Exposure to dust during annealing is especially problematic during the first anneal step, when the waveguide core is flowed. Any particles which settle on the core could be incorporated into it when the glass softens, making them impossible to remove. In addition, contaminants incorporated into the core cause higher scattering losses than particles on the surface because higher levels of optical power propagate in the core. If a large particle is incorporated into the core, it can result in the majority of the light escaping from the waveguide and thus in a defective device. Performing all the processing steps in a clean room environment should increase the overall device yield and reduce scattering losses.

5.2 Emitted Near Field Pattern Measurements

Fig. 5.4 depicts the setup used to capture images of the near-field pattern of the light emitted from the cleaved ends of the waveguides. Light was coupled into the waveguides using the technique described in Sec. 5.0. The light emitted from the waveguide was focused using a 40x microscope objective and expanded using a beam expander to produce a magnified image of the emitted near-field pattern. The output of the beam expander was imaged onto the detector of a CCD camera with the lens removed. The image generated by the camera was then captured using a frame grabber and the digital image processing software package IP Lab, running on a Macintosh computer.

Several precautions were necessary to achieve an accurate image of the emitted near-field pattern. First, light from the source fiber which was not coupled into the waveguide can propagate along the surface and interfere with the captured image. This was prevented by placing a small plastic block on top of the waveguide. Second, in order to minimize noise in the image from ambient light, the image capture was done in a darkened room. Third, to avoid saturating the detector and capturing a clipped image, the

power coupled into the waveguide was reduced by intentionally misaligning the source fiber.

Figure 5.5 is an intensity plot of the captured near-field image of a waveguide with an annealed upper cladding layer. The field is approximately Gaussian in both the x and y directions. Figures 5.6 A and B are intensity plots of slices in the x and y directions through the center of this image.

The image shown in Fig. 5.5 is quite noisy, but the general shape is essentially the same as the theoretical mode profile presented in Ch. 2. However, the full width half maximum (FWHM) measurements of the x and y slices through the mode profile are larger than was predicted by theoretical analysis. The line through the bottom of the x and y slices is the assumed background noise level. The difference between the captured image and the theoretical mode profile could be caused by several phenomena. First, phosphorous diffusion from the core into the cladding during the two annealing steps would increase the effective size of the core and increase the width of the mode profile. Second, deviations in the actual values of the refractive indices of the core and cladding from the values assumed in the theoretical analysis could result in a less confined mode than was predicted. Third, focusing errors or noise in the measurement could increase the apparent width of the mode. The difference observed is most likely due to a combination of these effects.

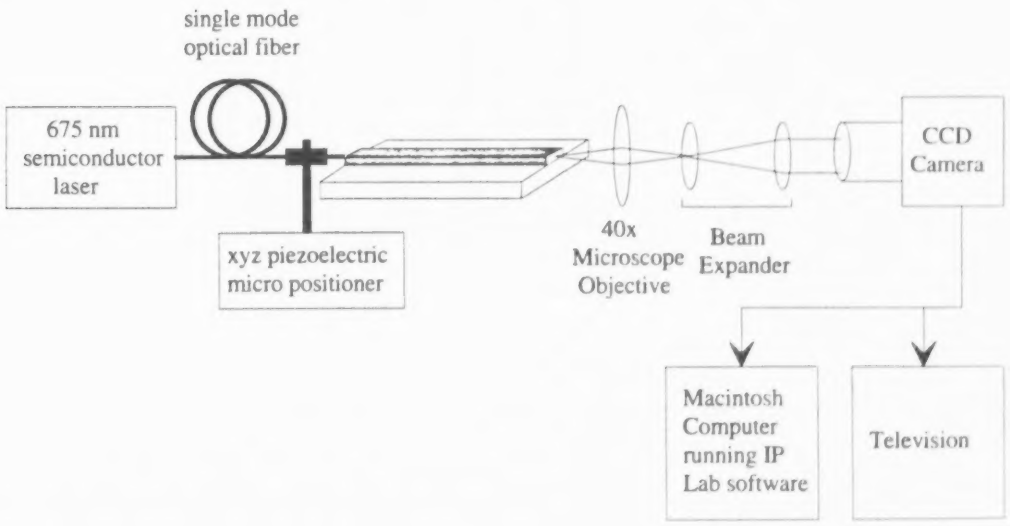

Figure 5.4 Waveguide Mode Profile Measurement Set Up

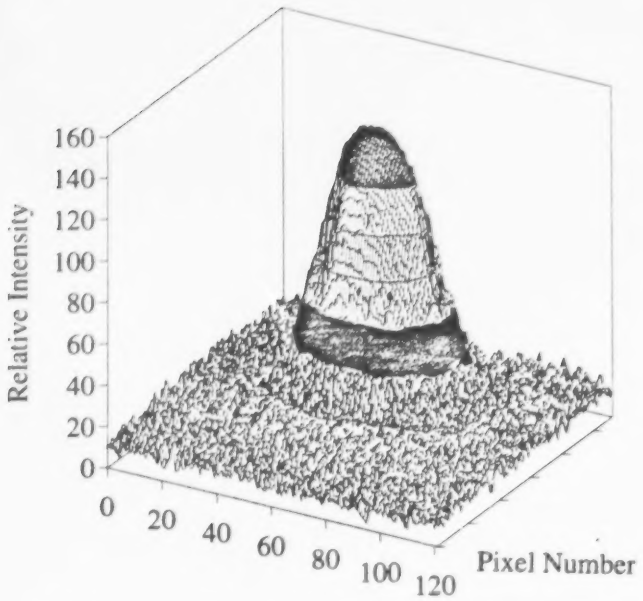

Figure 5.5 Intensity Plot of the Near-field Image of a Waveguide with an Annealed Upper Cladding Layer

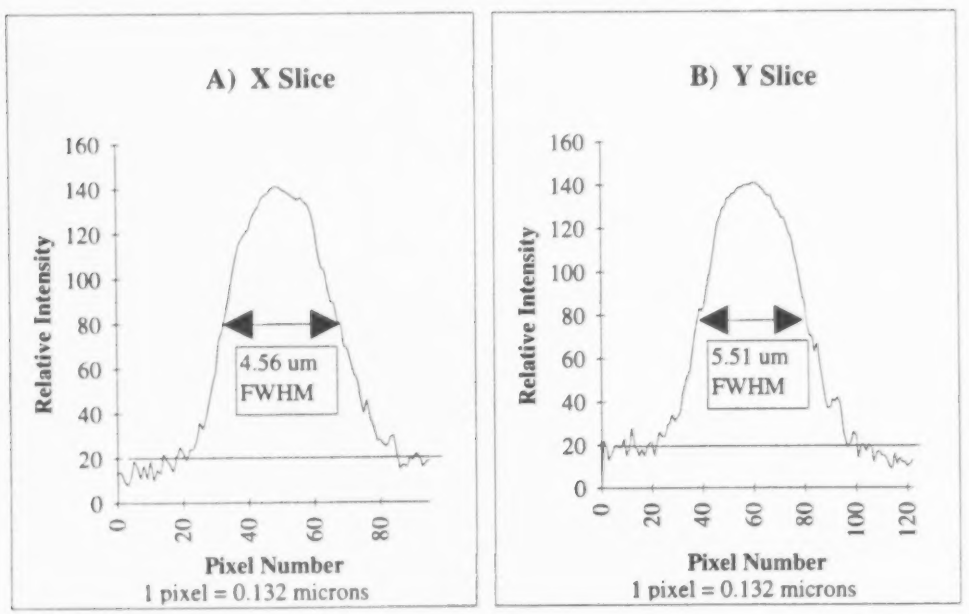

Figure 5.6 Intensity Plots of:

A) A Slice along the x-axis of the Image Shown in Figure 5.5

B) A Slice along the y-axis of the Image Shown in Figure 5.5

5.3 Emitted Optical Power versus Cantilever Displacement Measurements

The apparatus used to measure the optical power coupled out of the waveguide, as the cantilever's deflection was varied, is depicted in Fig. 5.7. Light was coupled into the waveguide as described in Sec. 5.0. The cantilever was displaced using a probe attached to a z-axis piezoelectric micropositioner mounted on a mechanical xyz micropositioner. Only cantilevers with an upward deflection were tested because the width of the probe was greater than the width of the cantilever opening. The cantilever could therefore only be deflected down until the probe touched the surface of the die. Light emitted from the device was collected using a plastic multimode fiber with a NA of 0.5. The plastic pickup fiber was butt-coupled to the waveguide and aligned using a mechanical micropositioner. Light from the source which is not coupled into the waveguide can propagate along the surface of the die and can be coupled into the waveguide opposite the cantilever or into the plastic pickup fiber. Similarly, light emitted from the cantilever which is not coupled into the waveguide across the gap can be coupled into the pickup fiber. These two noise sources were reduced by placing two small pieces of silicon on top of the waveguide immediately after the source and the gap. Also, in order to reduce noise from the ambient room light, all measurements were taken in a darkened room.

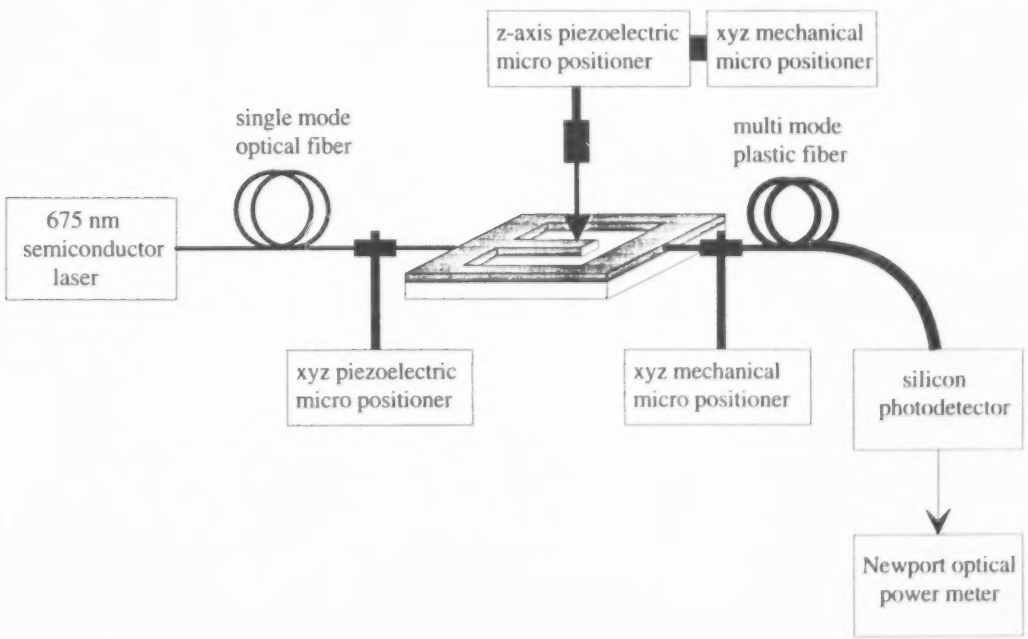

Figure 5.7 Cantilever Displacement Test Setup

Figure 5.8 is a plot of the detected optical power versus cantilever displacement for a cantilever with a 50 micron gap. A theoretical curve, based on the coupling analysis presented in Ch. 2, is also plotted on the same graph. The curves show reasonably good agreement, although the measured curve does not fall off as fast as the theoretical curve. This deviation could be due to the actual mode profile being wider than was assumed in the theoretical calculation. This hypothesis is supported by the measurements of the emitted mode profile presented in Sec. 5.2. The observed deviation could also be due to differences in the shape of the actual mode profile and assumed profile. For the case of a slab waveguide, the field in the cladding falls off with the relation exp(-kx). The Gaussian function used to approximate the mode falls off with the relation $\exp(-kx^2)$, much faster than the slab waveguide field. Despite the minor discrepancy between the measured and theoretical curves, Fig. 5.8 clearly shows that the optical output power of this device varies predictably with cantilever displacement and demonstrates the feasibility of the use of this device as an accelerometer.

Figure 5.8 Measured and Theoretical Power versus Displacement Curves of a Cantilever with a 50 micron gap

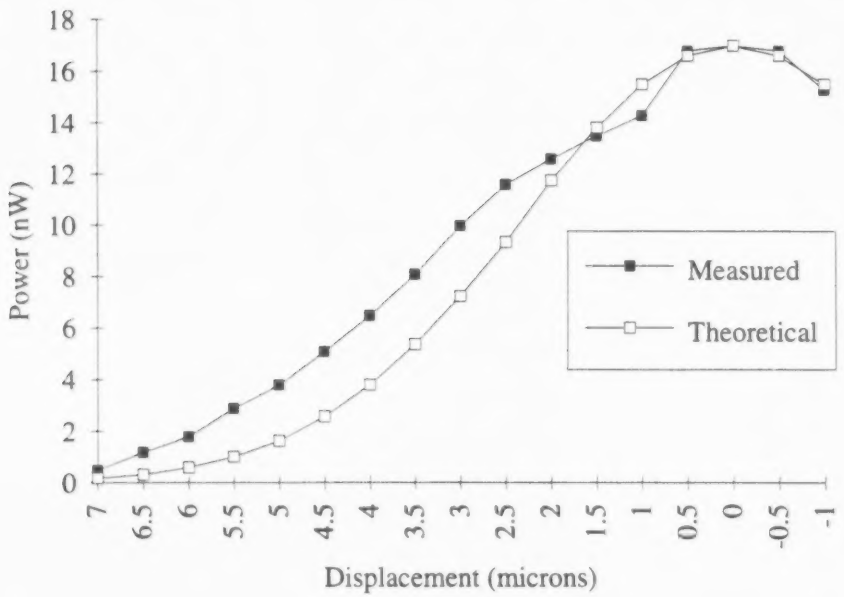

Figure 5.8 Measured and Theoretical Output Power versus Displacement for a Cantilever with a 50 μm Gap

The maximum output power of the waveguide cantilever was less than 18 nW, several orders of magnitude lower than the average output power of 95 μW measured for the waveguides in Sec. 5.1. The difference in output power is most likely due to a combination of coupling losses across the waveguide gap and increased scattering losses caused by core surface roughness resulting from the EDP etch step which is evident by comparing Fig. 4.7 and Fig. 4.11. Both of these loss mechanisms could probably be reduced by adding an additional anneal step after the EDP etch step, to reflow the waveguide core. Increasing the output power would give the device a greater measurement range and increase the loss from input and output fibers which could be tolerated.

6 CONCLUSIONS

In this thesis, the feasibility of fabricating an integrated optic accelerometer using the facilities of the Alberta Microelectronic Centre was investigated. The optical and mechanical properties of the device were modeled and a prototype device was fabricated and statically tested. The first step in the development of a prototype was the development of a single mode ridge waveguide fabrication process. This involved the development of a reactive ion etching process, SiO_2 and PSG deposition processes, as well as the modification of an existing photolithography process. Waveguides with low coupling losses to single mode fibers and estimated propagation losses of 0.2 dB/cm were demonstrated. A cantilever-waveguide fabrication process was then developed based on the waveguide process. Optical power versus displacement measurements were performed on a prototype cantilever waveguide. The results of this test demonstrated the feasibility of the device being used as an optical accelerometer.

Additional development work is required in several areas to bring the device developed for this thesis project to the level of a practical accelerometer. First, further experiments are needed to develop an annealing process which will minimize the bending of the cantilever beams. Modifications to the deposition processes to change the film stress level and distribution may also be required to minimize the cantilever bending. Second, the process should be modified to include the etching of v-grooves in the substrate for passive alignment of the input and output fibers and to facilitate the attachment of fibers to the device. Third, propagation losses in the cantilever waveguides must be reduced to increase the dynamic range of the device and to increase the input and output fiber loss that can be tolerated. The addition of a PSG reflow step to remove roughness in the waveguide core caused by the EDP etching step should reduce the losses. Performing the entire fabrication process in a clean room environment should also reduce the losses. Finally, dynamic testing of the device is required.

The single mode ridge waveguides developed for this project had low coupling and propagation losses and the potential exists for further improvements. There are a variety of other possible applications for these waveguides, such as optical interconnects for telecommunications devices and optical computers as well as other sensor applications such as optical gyroscopes or optical pressure sensors. In addition, the SiO_2 and PSG deposition processes as well as the annealing process developed for this work should be useful in the development of other types of waveguides and waveguide amplifiers.

REFERENCES

1.1 Puers B., Reynaert L., Snoeys W., Sansen M.C., "A New Uniaxial Accelerometer in Silicon Based on the Piezojunction Effect", IEEE Transactions on Electron Devices, Vol. 35, 1988, pp. 764-770

1.2 Igarashi I., "Semiconductor Dynamic Sensors", Sensors and Actuators, Vol. 13, 1988, pp. 53-62

1.3 Boxenhorn B., Greiff P., "Monolithic Silicon Accelerometer", Sensors and Actuators, Vol. A21-23, 1990, pp. 273-277

1.4 Rudolf F., Jornod A., Bergqvist J., Leuthold H., "Precision Accelerometers with micro g Resolution", Sensors and Actuators, Vol. A21-23, 1990, pp. 297-302

1.5 Seidel H., Riedel H., Kolbeck R., Muck G., Kupke W., Koniger M., "Capacitive Silicon Accelerometer with Highly Symmetrical Design", Sensors and Actuators, A21-23, 1990, pp. 312-315

1.6 Suzuki S., Tuchitani S., "Semiconductor Capacitance-type Accelerometer with PWM Electrostatic Servo Technique", Sensors and Actuators, Vol. A21-23, 1990, pp. 316-319

1.7 Wilner L., "A High Performance, Variable Capacitance Accelerometer", IEEE Transactions on Instrumentation and Measurement, Vol. 37, 1988, pp. 569- 571

1.8 Roylance L., Angell J. , "A Batch-Fabricated Silicon Accelerometer", IEEE Transactions on Electron Devices, Vol. ED-26, 1979, pp. 1911-1917

1.9 Burcham K., De Brabander G., Boyd J., "Micromachined Silicon Cantilever Beam Accelerometer Incorporating an Integrated Optical Waveguide", SPIE International Symposium: OE/Fibers Components Networks Sensors, Sept. 8-11, 1992, Boston Ma.

1.10 Wu S., Frankena H., "Micro-Mechanical Structures As Integrated Optical Sensor Elements", Integrated Photonics Research, Vol. 10, pp. 158-159, Optical Society of America Conference Proceedings, Washington DC, April 16, 1992

1.11 Bezzaoui H., Voges E., "Integrated Optics Combined with Micromechanics on Silicon", Sensors and Actuators, A, 29, 1991, pp. 219-223

2.1 Tamir T., "Integrated Optics", 2nd Ed., Springer-Verlag, Berlin, 1979

2.2 Technical Staff of CSELT, "Fiber Optic Communications Handbook", 2nd Ed., TAB Professional and Reference Books, Blue Ridge Summit, PA, 1990

2.3 Verdeyen J., "Laser Electronics", Prentice Hall, Englewood Cliffs, New Jersey, 1989

2.4 Nemoto S., Makimoto T., "Analysis of Splice Loss in Single-Mode Fibres Using A Gaussian Field Approximation", Optical and Quantum Electronics, Vol. 11, 1979, pp. 447-457

3.1 Rao Singiresu S., "Mechanical Vibrations", 2nd Ed., Addison-Wesley, 1990
3.2 Clough Ray W. and Penzien, Joseph, "Dynamics of Structures", McGraw-Hill, 1975
3.3 Timoshenko S., "Vibration Problems in Engineering, 3rd Ed., D. Van Nostrand Company, Inc., 1955
3.4 Petersen Kurt E., Guarnieri, C. R., "Young's Modulus Measurements of Thin Films Using Micromechanics", J. Appl. Phys. 50, 1979, pp 6761-6766
3.5 Jaccodine R. J., Schlegel, W. A., "Measurement of Strains at Si-SiO2 Interface", J. Appl. Phys. 37, 1966, pp 2429-2434
3.6 Jackson C., "The Practical Vibration Primer", Gulf Publishing Company, 1979, p.5
3.7 D'Azzo J., Houpis C., "Linear Control System Analysis & Design", 3rd Ed., McGraw-Hill, 1988

4.1 Technical Staff of CSELT, "Fiber Optic Communication Handbook", p. 69
4.2 Takamatsu A., Shibata M., Sakai H., and Yoshimi T., "Plasma Activated Deposition and Properties of Phosphosilicate Glass Film", J. Electrochem. Soc.,Vol 131, 1984, pp. 1865-1870
4.3 Simko J., Oehrlein G., "Reactive Ion Etching of Silicon and Silicon Dioxide in CF4 Plasmas Containing H2 or C2F4 Additives", J. Electrochem. Soc.,Vol 136, 1991, pp. 2748-2752
4.4 Baret G., Madar R., and Bernard C., "Silica-Based Oxide Systems I. Experimental and Calculated Phase Equilibria in Silicon, Boron, Phosphorus, Germanium, and Arsenic Oxide Mixtures", J. Electrochem. Soc.,Vol 138, No. 9, Sept. 1991, pp. 2830-2835
4.5 Baret G., Madar R., and Bernard C., "Silica-Based Oxide Systems II. Determination of Silica-Based, Low Flow Temperature Glasses for Electronic Applications from Relations Between Glass Transition, Flow and Liquidus Temperatures", J. Electrochem. Soc.,Vol 138, No. 9, Sept. 1991, pp. 2836-2838
4.6 Naumaan A., Boyd J., "Phosphosilicate Glass Flow for Integrated Optics", J. Vac. Sci. Technol., Vol. 17, No. 1, Jan./Feb. 1980, pp. 529-532
4.7 Barry M., "Doped Oxides as Diffusion Sources", J. Electrochem. Soc.: Solid-State Science and Technology, Vol. 117, 1970, pp. 1405-1410
4.8 Ghezzo M., Brown D., "Diffusivity Summary of B, Ga, P, As, and Sb in SiO2",

J. Electrochem. Soc.: Solid-State Science and Technology, Vol. 120, 1972, pp. 146-148

4.9 "AMC Silicon Micromachining Short Course Manual", Feb. 5, 1991, Internal Document

4.10 Ho C., Hansen S., and Fahey P., "SUPREM III, A Program for Integrated Circuit Process Modeling and Simulation", Technical Report No. SEL 84-001, Stanford University, CA, USA, 1984

5.1 Narendra R., McMullin J., "Single Mode, Phosphorus-Doped Silica Waveguides in Silicon V-Grooves", IEEE Photonics Tech. Letters, Vol. 5, No. 1, Jan. 1983

5.2 Imoto K., Sano H., and Miyazaki M., "Guided-wave multi/demultiplexers with high stop band rejection", Applied Optics, Vol. 26, No. 19, Oct. 1 1987, pp. 4214-4219

5.3 Takato N., Jinguji K., Yasu M., Toba H., and Kawachi M., "Silica Based Single Mode Waveguides on Silicon and their Applications to Guided-Wave Optical Interferometers", J. Lightwave Tech., Vol. 6, No. 6, June 1988, pp. 1003-1009

5.4 Boyd J., Wu R., Zelmon D., Naumaan A., and Timlin H., "Guided wave optical structures utilizing silicon", Optical Engineering, Vol. 24, No. 2, March 1985, pp. 230-234

5.5 Naumaan A. and Boyd J., "Ring Resonator Fabricated in Phosphosilicate Glass Films Deposited by Chemical Vapor Deposition", J. Lightwave Tech., Vol. 4, No. 9, Sept. 1986, pp. 1294-1303

5.6 Verbeek B., Henry N., Olsson K., Orlowsky R., Kazarinov R., and Johnson B., "Integrated Four-Channel Mach-Zehnder Multi/Demultiplexers Fabricated with Phosphorous Doped SiO2 Waveguides on Si", J. Lightwave Tech., Vol. 6, No. 6, June 1988, pp. 1011-1015

5.7 Valette S., Gidon P., Renard S. and Jadot J., "Silicon Based Integrated Optics Technology: An Attractive Hybrid Approach for Optoelectronics", SPIE Vol. 1128, 1989, pp. 179-185

5.8 Hickernell F., "Optical Waveguides on Silicon", Solid State Tech., Nov. 1989, pp. 83-88